J. Fluid Mech. (2012), *vol.* 710, *pp.* 569–605.
doi:10.1017/jfm.2012.377

A throttling mechanism sustaining a hole tone feedback system at very low Mach numbers

K. Matsuura[1]† and M. Nakano[2]

[1] Graduate School of Science and Engineering, Ehime University, 3 Bunkyo-cho, Matsuyama, Ehime, 790-8577, Japan

[2] Institute of Fluid Science, Tohoku University, 2-1-1 Katahira, Aoba-ku, Sendai, Miyagi, 980-8577, Japan

(Received 6 October 2011; revised 22 May 2012; accepted 21 July 2012; first published online 3 September 2012)

This study investigates the sound produced when a jet, issued from a circular nozzle or hole in a plate, goes through a similar hole in a second plate. The sound, known as a hole tone, is encountered in many practical engineering situations. Direct computations of a hole tone feedback system were conducted. The mean velocity of the air jet was 10 m s^{-1}. The nozzle and the end plate hole both had a diameter of 51 mm, and the impingement length between the nozzle and the end plate was 50 mm. The computational results agreed well with past experimental data in terms of qualitative vortical structures, the relationship between the most dominant hole tone peak frequency and the jet speed, and downstream growth of the mean jet profiles. Based on the computational results, the shear-layer impingement on the hole edge, the resulting propagation of pressure waves and the associated vortical structures are discussed. To extract dominant unsteady behaviours of the hole tone phenomena, a snapshot proper orthogonal decomposition (POD) analysis of pressure fluctuation fields was conducted. It was found that the pressure fluctuation fields and the time variation of mass flows through the end plate hole were dominantly expressed by the first and second POD modes, respectively. Integrating the computational results, an axisymmetric throttling mechanism linking mass flow rates through the hole, vortex impingement and global pressure propagation, is proposed.

Key words: absolute/convective instability, aeroacoustics, jets

1. Introduction

The sound produced when a jet, issued from a circular nozzle or hole in a plate, goes through a second plate that has a hole of the same diameter is referred to as a hole tone. The tone is encountered in many situations such as solid propellant rocket motors, automobile intakes and exhaust systems, ventilation systems, gas distribution systems, and whistling kettles, etc. The hole tone is categorized as a fluid dynamic self-excited oscillation where axisymmetric coherent vortices are produced in the naturally unstable jets, convected downstream, and the generation and feedback of induced disturbances occur from some point in the flow near the surface on which the vortices are impinging (Rayleigh 1945; Blake 1986; Howe 1997*a*; Ginevsky, Vlasov & Karavosov 2010). Jet tone phenomena similar to the hole tone, involving impinging

† Email address for correspondence: matsuura.kazuo.mm@ehime-u.ac.jp

surfaces, include edge and ring tones (Rockwell & Naudascher 1979; Blake 1986; Ginevsky *et al.* 2010). The interaction of the jet shear layer and the surface gives rise to strong self-excited oscillations with frequencies determined by the flow speed, the initial thickness of the mixing layer, and the distance from the nozzle edge downstream to the obstacle (Ginevsky *et al.* 2010).

Sondhauss (1854) first reported on the hole tone in 1854 and found that the tone frequency increased with increasing jet velocity, and decreased with increasing distance between the orifices. Rayleigh (1945, pp. 410–412), based on his observations, conjectured a mechanism, now known as a feedback mechanism (Rayleigh 1945; Rossiter 1962; Chanaud & Powell 1965; Rockwell & Naudascher 1979), as follows: 'When a symmetrical excrescence reaches the second plate, it is unable to pass the hole with freedom, and the disturbance is thrown back, probably with the velocity of sound, to the first plate, where it gives rise to a further disturbance, to grow in its turn during the progress of the jet.' In the mechanism, as a result of the axisymmetric instabilities of the jet, each vortex is convected over the gap L_{im} during a time of the order of L_{im}/u_c, at the shear-layer convection velocity u_c, which is typically about half the mean jet speed at exit u_0. An impulsive disturbance is generated when the vortex impinges on the downstream edge which initiates the formation of a new vortex. The impulse takes a finite time $\sim L_{im}/c_\infty$ to travel back across the gap, where c_∞ is the speed of sound. Based on this picture, the frequency f of the vortex formation satisfies $n/f \sim L_{im}/u_c + L_{im}/c_\infty$, where the values $n = 1, 2, 3$, etc., correspond to the various stages of operation (Rossiter 1962). Crighton (1992) presented a linear analytical model to predict the frequency characteristics of the discrete oscillations of the jet-edge feedback cycle. Problems corresponding to various physical processes associated with the cycle are analysed, for inviscid flows with vortex-sheet shear layers and aligned flat-plate boundaries, and solved in an appropriate asymptotic sense by Wiener–Hopf methods. Holger (1977) proposed a model for an edge tone that consists of a periodic disturbance at a jet origin leading to the formation of an asymmetric vortex street, and a potential flow analysis of the interaction of the vortices with the edge to calculate the phase of the feedback mechanism. Howe (1997*b*) conducted linearized analyses of self-sustaining oscillations of high-Reynolds-number shear layers and jets incident on edges and corners at an infinitesimal Mach number. In the study, the operating stages of self-sustained oscillations are identified with poles, in the upper half of the complex frequency plane, of the Rayleigh conductivity $K_R(\omega)$, by which the volume flux $Q(t)$ through the aperture is determined by the equation

$$\rho_0 \frac{\partial Q(t)}{\partial t} = -\int_{-\infty}^{\infty} K_R(\omega)[p_0(\omega)]\mathrm{e}^{-\mathrm{i}\omega t}\,\mathrm{d}\omega. \tag{1.1}$$

Here, $[p_0(t)] \equiv p_+(t) - p_-(t)$ is a uniform, time-dependent pressure differential linearly disturbing the shear layer over the aperture, $p_\pm(t)$ are uniform pressures applied, respectively, above and below the wall, and ω is the complex frequency. Umeda & Ishii (1986) conducted experimental studies on the hole tone with supersonic jets, and visualized six different sound wave propagations by shadow-graph pictures. They observed two different processes in the generation of sound waves: (i) a feedback mechanism consisting of sound waves propagating upstream outside the jet that trigger downstream-convecting coherent vortical structures surrounding the jet upstream of the second plate; and (ii) radial expansion of the vortical structures when they are created and merged downstream of the second plate. Langthjem & Nakano (2005) proposed a numerical approach to the generation of hole tones based on a discrete vortex method using axisymmetric vortex rings combined with an acoustic feedback mechanism based

on a simplified Curle's equation where only dipoles and monopoles are retained. The dipoles and monopoles are evaluated respectively by the fluid force acting on the upstream surface of the end plate, and by the time derivative of velocity at the hole inlet position. The acoustic velocity potential function is obtained by integrating the solution of the equation. Acoustic velocities obtained by differentiating the potential function by the coordinate are added to the hydrodynamic velocity field near the nozzle exit as the feedback effect.

Despite the long history of the hole tone problem, a comprehensive analytical/numerical solution has not yet been developed. Recently, Matsuura & Nakano (2011) conducted, to the best of their knowledge, the first direct computations of a hole tone feedback system at very low Mach numbers $Ma \sim 0.029$, which predicted its dominant frequency successfully. They discussed the shear-layer impingement on the hole edge, the resulting propagation of pressure waves, and the associated vortical structures. In the study, a new feedback mechanism was found, based on the computed results, for an air jet speed of 10 m s^{-1}. It has been believed for some time that pressure waves outside the jet trigger the feedback of the hole tone, whereas pressure waves also pass inside the jet for the feedback, and the jet including its shear layers oscillates periodically. However, the details of the origin of the generation of pressure waves were unknown.

In this study, direct computations of a hole tone feedback system were conducted to investigate the origin. The mean velocity of the air jet was 10 m s^{-1}. The diameters of the nozzle and the end plate hole were both 51 mm, and the impingement length between the nozzle and the end plate was 50 mm. In § 2, numerical methods, computational conditions, grids, initial and boundary conditions are described. In § 3, the periodicity of the computed phenomena is assessed, and the validation studies of these computations against past experimental measurements (Matsuura & Nakano 2011) are conducted in terms of qualitative vortical structures, the relationship between the most dominant hole tone peak frequency and the jet speed, and the downstream growth of the mean jet profiles. In § 4, based on the computational results, the shear-layer impingement on the hole edge, the resulting propagation of pressure waves and associated vortical structures are discussed. In § 5, a snapshot proper orthogonal decomposition (POD) analysis of pressure fluctuation fields is conducted in order to extract dominant unsteady behaviours of the hole tone phenomena. In § 6, integrating the computational results, an axisymmetric throttling mechanism linking the mass flow rates through the hole, the vortex impingement and global pressure propagation is proposed. In § 7, conclusions for this study are drawn. In appendix A, a simple explanation for the generation of a high pressure region and the directions of vorticity vectors between two low pressure regions with backflows are given based on potential flow theory. In appendix B, the method of evaluation of instantaneous acoustic power is explained.

2. Numerical analysis

2.1. *Numerical method*

The governing equations are the unsteady three-dimensional fully compressible Navier–Stokes equations in general coordinates (ξ, η, ζ), written in conservative variables and expressed in the following notational form:

$$\frac{\partial \boldsymbol{Q}}{\partial t} + \frac{\partial}{\partial \xi}(\boldsymbol{F} - \boldsymbol{F}_v) + \frac{\partial}{\partial \eta}(\boldsymbol{G} - \boldsymbol{G}_v) + \frac{\partial}{\partial \zeta}(\boldsymbol{H} - \boldsymbol{H}_v) = \boldsymbol{S}. \tag{2.1}$$

The vector of the conservative variables is given by

$$\boldsymbol{Q} \equiv \frac{1}{J}\left(\rho,\, \rho u_1,\, \rho u_2,\, \rho u_3,\, \rho e\right)^t . \tag{2.2}$$

Here, J is the Jacobian, ρ is the density, u_1, u_2, u_3 are the velocity components in Cartesian coordinates, and e is the total energy per unit mass. The inviscid and viscous vector fluxes, i.e. $\boldsymbol{F}, \boldsymbol{G}, \boldsymbol{H}$ and $\boldsymbol{F}_v, \boldsymbol{G}_v, \boldsymbol{H}_v$, respectively, are given by

$$\left.\begin{aligned} \boldsymbol{F} &\equiv \frac{1}{J}\begin{pmatrix} \rho U_1 \\ \rho u_1 U_1 + \xi_x p \\ \rho u_2 U_1 + \xi_y p \\ \rho u_3 U_1 + \xi_z p \\ \rho e U_1 + \xi_{x_i} u_i p \end{pmatrix}, \quad \boldsymbol{G} \equiv \frac{1}{J}\begin{pmatrix} \rho U_2 \\ \rho u_1 U_2 + \eta_x p \\ \rho u_2 U_2 + \eta_y p \\ \rho u_3 U_2 + \eta_z p \\ \rho e U_2 + \eta_{x_i} u_i p \end{pmatrix}, \\ \boldsymbol{H} &\equiv \frac{1}{J}\begin{pmatrix} \rho U_3 \\ \rho u_1 U_3 + \zeta_x p \\ \rho u_2 U_3 + \zeta_y p \\ \rho u_3 U_3 + \zeta_z p \\ \rho e U_3 + \zeta_{x_i} u_i p \end{pmatrix}, \end{aligned}\right\} \tag{2.3}$$

$$\left.\begin{aligned} \boldsymbol{F}_v &\equiv \frac{1}{J}\begin{pmatrix} 0 \\ \xi_{x_i}\sigma_{i1} \\ \xi_{x_i}\sigma_{i2} \\ \xi_{x_i}\sigma_{i3} \\ \xi_{x_i}[u_j\sigma_{ij} - Q_i] \end{pmatrix}, \quad \boldsymbol{G}_v \equiv \frac{1}{J}\begin{pmatrix} 0 \\ \eta_{x_i}\sigma_{i1} \\ \eta_{x_i}\sigma_{i2} \\ \eta_{x_i}\sigma_{i3} \\ \eta_{x_i}[u_j\sigma_{ij} - Q_i] \end{pmatrix}, \\ \boldsymbol{H}_v &\equiv \frac{1}{J}\begin{pmatrix} 0 \\ \zeta_{x_i}\sigma_{i1} \\ \zeta_{x_i}\sigma_{i2} \\ \zeta_{x_i}\sigma_{i3} \\ \zeta_{x_i}[u_j\sigma_{ij} - Q_i] \end{pmatrix}, \end{aligned}\right\} \tag{2.4}$$

where $(x, y, z) = (x_1, x_2, x_3)$ are Cartesian coordinates, the contravariant velocity components U_1, U_2, U_3 are defined by metrics ξ_i, η_i, ζ_i $(i = x, y, z)$ as

$$U_1 \equiv \xi_x u_1 + \xi_y u_2 + \xi_z u_3, \tag{2.5a}$$

$$U_2 \equiv \eta_x u_1 + \eta_y u_2 + \eta_z u_3, \tag{2.5b}$$

$$U_3 \equiv \zeta_x u_1 + \zeta_y u_2 + \zeta_z u_3, \tag{2.5c}$$

and p is the static pressure. The total energy per unit volume ρe is expressed as

$$\rho e = \frac{p}{(\gamma - 1)} + \frac{1}{2}\rho(u_1^2 + u_2^2 + u_3^2), \tag{2.6}$$

where γ is the specific heat ratio. The components of the viscous stress tensor $\sigma_{ij}(i, j = 1, \ldots, 3)$ and the heat flux vector $Q_i(i = 1, \ldots, 3)$ are defined by

$$\sigma_{ij} \equiv \mu\left(\frac{\partial \xi_k}{\partial x_j}\frac{\partial u_i}{\partial \xi_k} + \frac{\partial \xi_k}{\partial x_i}\frac{\partial u_j}{\partial \xi_k} - \frac{2}{3}\delta_{ij}\frac{\partial \xi_l}{\partial x_k}\frac{\partial u_k}{\partial \xi_l}\right), \tag{2.7}$$

$$Q_i \equiv -\lambda\frac{\partial \xi_j}{\partial x_i}\frac{\partial T}{\partial \xi_j}, \tag{2.8}$$

where μ is the viscosity, λ is the thermal conductivity, T is the temperature and $\delta_{ij}(i, j = 1, \ldots, 3)$ is Kronecker's delta function. The perfect gas law closes the system of equations

$$p = \rho RT, \tag{2.9}$$

where R is the gas constant. Sutherland's formula for viscosity is adopted and a constant Prandtl number of $Pr = 0.72$ is assumed. $\boldsymbol{S}$ in (2.1) is zero except for the inlet sponge region, which is mentioned later in § 2.2.

The equations were solved using the finite-difference method. Spatial derivatives that appeared in the metrics, convective and viscous terms were evaluated by the sixth-order tridiagonal compact scheme (Lele 1992). Near boundaries, the fourth-order one-sided and classical Padé schemes (Lele 1992) are used at the boundaries and one point internal to them. Time-accurate solutions to the governing equations were obtained using the third-order explicit Runge–Kutta scheme. The time increment was constant and $\Delta t = 2.4 \times 10^{-4} L_{im}/c_\infty$ in all flow fields. The Courant–Friedrichs–Lewy (CFL) numbers of these computations, which were defined by the maximum sums of the contravariant velocity and the speed of sound scaled by the metrics as

$$CFL \equiv \Delta t \max(|U_1| + c_\infty \sqrt{\xi_{x_i}\xi_{x_i}}, |U_2| + c_\infty \sqrt{\eta_{x_i}\eta_{x_i}}, |U_3| + c_\infty \sqrt{\zeta_{x_i}\zeta_{x_i}}), \tag{2.10}$$

were around 0.4. In addition to the above-mentioned spatial discretization and time integration, a tenth-order implicit filtering (Gaitonde & Visbal 2000) was introduced to suppress numerical instabilities that arise from central differencing in the compact scheme:

$$\alpha_f \hat{\phi}_{i-1} + \hat{\phi}_i + \alpha_f \hat{\phi}_{i+1} = \sum_{n=0}^{5} \frac{a_n}{2}(\phi_{i+n} + \phi_{i-n}), \quad i \in \{6, \ldots, i_{max} - 5\}. \tag{2.11}$$

Here, ϕ denotes a conservative quantity and $\hat{\phi}$ a filtered quantity at each grid point. Regarding coefficients a_n $(n = 0, \ldots, 5)$, the values in Gaitonde & Visbal (2000) are used. The filter parameters α_f that appear on the left-hand side are set to 0.33 for $i = 2$ and $i_{max} - 1$, 0.492 for $2 < i < i_{max} - 1$. Near the boundaries, implicit filters of orders $p = (4, 4, 6, 8, 10)$th for $i = (2, \ldots, 6)$ and $i = (i_{max} - 1, \ldots, i_{max} - 5)$, are used. Here, $i \in \{k, l\}$, and indices j, k, l respectively run in the circumferential θ, radial r and streamwise z directions in the general coordinate system. Not only the accuracy of the filter but also the value of α_f had a considerable influence both on the accuracy and stability of the calculation. In this study, the above value was used to keep the stability of the calculation while maintaining the high accuracy of the computational results. Regarding the computation of the linear algebraic equation, the Thomas algorithm was used for the tridiagonal systems, and the Sherman–Morrison formula (Press *et al.* 1992) was used for the cyclic tridiagonal systems that appear in the exact periodic treatment in the θ direction described in the next subsection. This numerical method has been well validated for the prediction of transitional and turbulent subsonic flows (Matsuura & Kato 2007).

2.2. *Computational details*

Figure 1 shows the computational overview of this problem. The diameters of the nozzle and the end plate hole were both $d_0 = 51$ mm. In the numerical model, the outer diameter of the end plate was taken to be 250 mm. The reference gap length (or impingement length) L_{im} was 50 mm. This computation assumed the standard atmospheric conditions, i.e. a temperature of 20 °C and a pressure of 1 atm as the

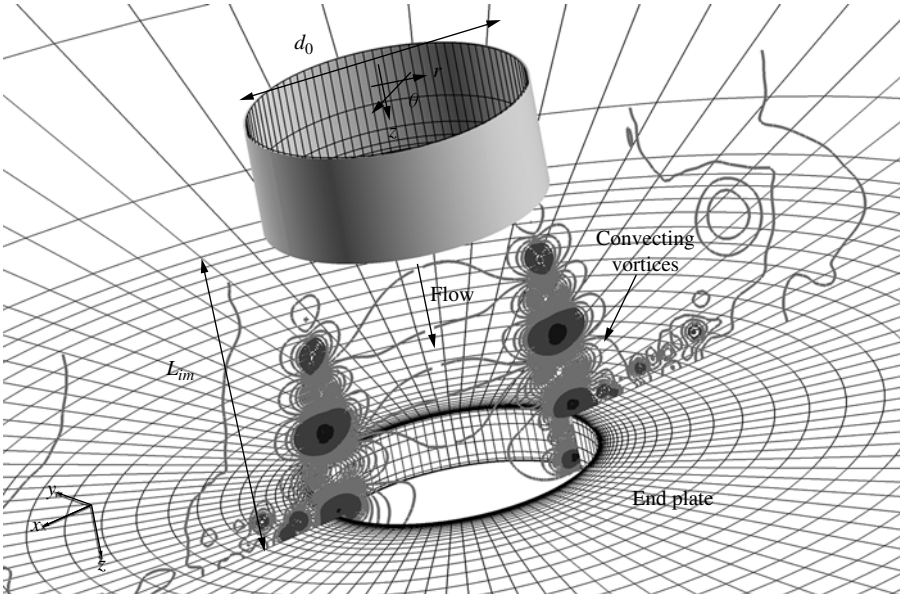

FIGURE 1. Hole tone system: an instantaneous pressure field in a computation when $u_0 = 10$ m s^{-1} (Matsuura & Nakano 2011).

ambient conditions. The reference mean velocity u_0 of the air jet is 10 m s^{-1}. At 20 °C, $u_0 = 10$ m s^{-1} corresponds to a Reynolds number $Re = u_0 d_0/\nu = 3.39 \times 10^4$ and a Mach number $Ma = u_0/c_\infty = 0.029$, where the speed of sound $c_\infty = 343$ m s^{-1} and the kinematic viscosity $\nu = 1.51 \times 10^{-5}$ m^2 s^{-1}. Figure 2 shows an overview of the computational grid consisting of five zones. Cylindrical-coordinate grids (r, θ, z) of the O-type topology are generated in each zone. $z = 0$ mm corresponds to the nozzle exit. Exact overlapping of five grid lines in the normal direction to an interface, which corresponds to 'a, b, c, d, e' in figure 2, is used between neighbouring zones. The details of overlapping for 'b' are shown in the enlarged figure. The $z = 0$ plane outside the nozzle in figure 2 is modelled as a wall, which is consistent with a corresponding experimental system shown in figure 4 of Matsuura & Nakano (2011). The nozzle exit plate is removed in figure 1 for clarity.

Periodicity in the θ direction is treated strictly without employing a one-sided biased scheme near the branch cut with regard to the derivative and filtering scheme. This O-type topology has a singularity at the centreline. To circumvent this, primitive values, circumferentially averaged at $k = 2$, are inserted into the primitive values at $k = 1$, i.e. $f_{j,1,l} = \sum_{i=1}^{j_{max}-1} f_{i,2,l}/(j_{max} - 1)$, $\forall (j, l) \in \{1, \ldots, j_{max}\} \times \{1, \ldots, l_{max}\}$. The total number of grid points is initially 1.17×10^6 points denoted as 'grid A' or '1M grid', and increased up to 9.07×10^6 points denoted as 'grid B' or '9M grid'. Computations with grid B give improved results in terms of the most dominant hole tone peak frequency as found by the frequency of 330 Hz mentioned later in § 3, and the results of grid A and the experimental data in figure 7 of Matsuura & Nakano (2011). Grid B also gives improved velocity profiles in the jet shear layers mentioned later in figure 9. Therefore, the results of mainly grid B are discussed in this paper. The results of grid A are used for mesh refinement tests and for generating an initial condition for

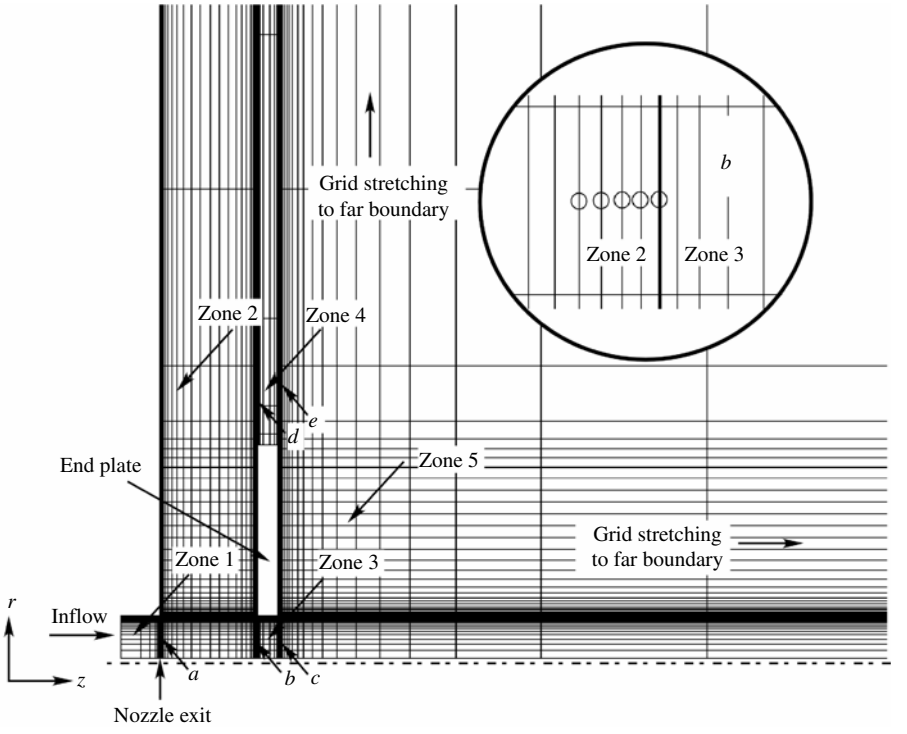

FIGURE 2. Computational grid for $\theta = 0$ rad (Matsuura & Nakano 2011). Every five grid lines in the r and z directions are drawn.

the computation of grid B. Grid A is also used for the evaluation of instantaneous acoustic power in appendix B.

The distribution of grid widths in the radial (r), circumferential (θ) and streamwise (z) directions between the nozzle exit and the end plate, inside the hole and downstream of the hole is shown in figure 3 of Matsuura & Nakano (2011). Mesh widths are made fine so as to capture jet shear layers accurately in the r direction, and in the separation regions near both the nozzle exit and the end plate hole in the r and z directions. The maximum grid widths Δ_{max} in the z direction between the nozzle exit and the end plate are $\Delta_{max} \sim 2.84$ mm in grid A and ~ 1.00 mm in grid B. The minimum grid widths Δ_{min}/d_0 are 1×10^{-3} in grid A and 4.9×10^{-4} in grid B. In this study, the outer region of jets between the nozzle exit and the end plate is laminar or in an initial stage of transition (Matsuura & Nakano 2011). Therefore, dominant/coherent structures under these flow features with global instability are expected to be well predicted by a relatively small number of grid points if the dispersion error is kept as low as possible.

Regarding the boundary conditions, the sponge layer method (Freund 1997), which specifies inflow velocity profiles consistent with experimental data, is used near the nozzle inlet, i.e. $\Omega_{z,in} = [d_0/51, d_0/2] \times [0, 2\pi) \times [-d_0/2.55, -d_0/10.2]$. Figure 3 shows the measured velocity profiles of the boundary layers at $(\theta, z) = (0 \text{ rad}, 0 \text{ mm})$ by a hot wire and a Pitot probe for $u_0 = 8$, 10 and 12 m s^{-1} when free jets are considered without the downstream end plate, and the computational inflow velocity profile for $u_0 = 10$ m s^{-1}. The hot wire is used within 4 mm of the wall, and the Pitot probe is

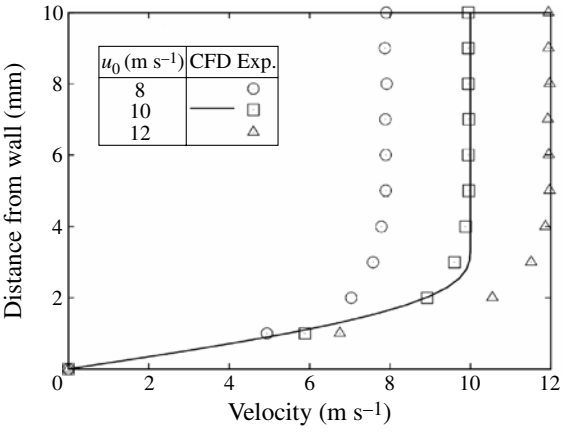

FIGURE 3. Comparison of experimental ('Exp.') and computational ('CFD') inflow boundary layer velocity profiles: $u_0 = 8$, 10 and 12 m s^{-1} for the experiments, and $u_0 = 10$ m s^{-1} for the computation.

used elsewhere. The inflow boundary layers for $u_0 = 8$, 10 and 12 m s^{-1} are laminar in the experiment (Matsuura & Nakano 2011). For implementation of the sponge layer, $\boldsymbol{S}$ in (2.1) is set to

$$\boldsymbol{S} = -c(z)(\boldsymbol{Q} - \boldsymbol{Q}_{targ}). \tag{2.12}$$

Here, $c(z)$ is a coefficient defined by

$$c(z) = c_1 r^{c_2}, \quad r_1 = \frac{z - z_e}{l_s}, \quad l_s = |z_s - z_e|, \tag{2.13}$$

$$c_1 = 9.28 \times 10^4, \quad c_2 = 2, \tag{2.14}$$

$$z_e = -5 \text{ mm}, \quad z_s = -d_0/2.55. \tag{2.15}$$

$\boldsymbol{Q}_{targ}$ is the target conservative variables defined by

$$\boldsymbol{Q}_{targ} \equiv \left(\rho_\infty, 0, 0, \rho_\infty w_{infl}, \frac{p_\infty}{\gamma - 1} + \frac{1}{2}\rho_\infty w_{infl}^2\right), \tag{2.16}$$

where w_{infl} is the inflow velocity profile mentioned above. Here, ∞ denotes the standard atmospheric conditions. In the sponge region, the root mean squares of pressure fluctuations at $(r, z) = (12.2, -10.0)$ and $(12.2, -15.2)$ are 2.26×10^{-2} Pa and 8.24×10^{-5} Pa, respectively, and the pressure waves are well attenuated. In the notation above, (r, z) implicitly means $\theta = 0$, which is now used in this paper. In this system where global instability is taking place, shear layers near the nozzle exit are perturbed by periodically propagating pressure waves with natural oscillation frequencies. To avoid disrupting naturally oscillating structures, no excitation such as random forcing is imposed at the inlet boundary. Although some fundamental convective instability of round jets is well known (Michalke 1984), little is known at present about the effects of inlet disturbances on the hole tone and they will be investigated in the future.

Far boundaries are set at $\Omega_{z,ex} = [d_0/51, 41.7d_0] \times [0, 2\pi) \times [41.4d_0, 41.4d_0]$ and $\Omega_{r,ex} = [41.7d_0, 41.7d_0] \times [0, 2\pi) \times [0, 41.4d_0]$. Figure 4(*a*,*b*) shows the distribution of

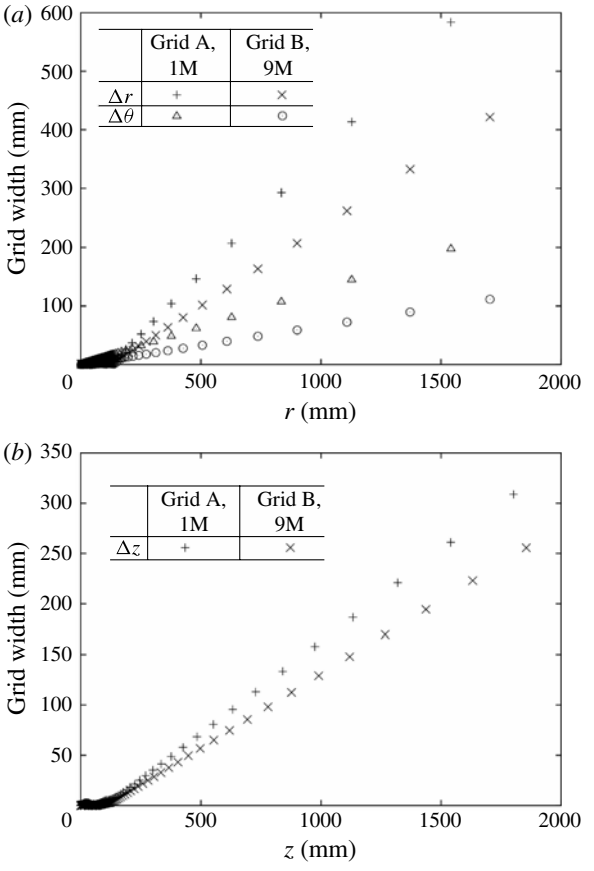

FIGURE 4. Distribution of grid widths in the r, θ, z directions near the far boundaries ($z = 0$ mm: nozzle exit): (a) r, θ directions, (b) z direction.

grid widths in the r, θ and z directions near the far boundaries. At the far boundaries, grid stretching similar to the methodology of Rai & Moin (1993) is used. Figure 5 shows the standard deviations p'' of pressure variations $p(t)$ ($145.4 \leqslant t^* \leqslant 290.2$) along the segments $60 \leqslant z \leqslant 41.4d_0$ of $r = \text{const.}$ for the flow field data saved every 3000 steps after the flow field reaches equilibrium. t^* is the time non-dimensionalized by L_{im} and c_∞, and $145.4 \leqslant t^* \leqslant 290.2$ corresponds to 200 saved data; t^* is mentioned in detail later in § 3.

Here, p'' is defined by

$$p'' \equiv \sqrt{\frac{1}{N_{max}} \sum_{i=1}^{N_{max}} (p(t_i) - \overline{p})^2}, \quad \overline{p} \equiv \frac{1}{N_{max}} \sum_{i=1}^{N_{max}} p(t_i), \quad N_{max} = 200. \tag{2.17}$$

In the z direction, p'' near $(r, z) = (25.5 \text{ mm}, 1000 \text{ mm})$ is attenuated to less than $\sim 1/49$ of the maximum p'' near the jet shear layer immediately downstream of the hole, i.e. $(r, z) \sim (25.5 \text{ mm}, 60 \text{ mm})$. In the r direction, p'' at $r \sim 1371$ mm is attenuated to less than $\sim 1/82$ of the maximum p''. Thus, pressure fluctuations are well

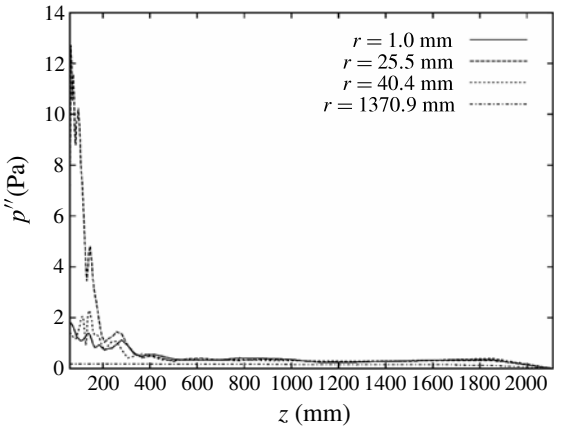

FIGURE 5. Standard deviations p'' of pressure variations along the segments $60 \leqslant z \leqslant 41.4d_0$ of $r = \text{const.}$

attenuated in the grid-stretched regions and therefore the effects of reflection from the far boundaries are negligible.

As an initial condition for the computation with grid A, a base profile and uniform random numbers $\epsilon_i \in [-1, 1], \forall i \in (1, \ldots, 3)$ for breaking symmetry are employed:

$$(\rho, u_r, u_\theta, u_z, p) = \begin{cases} (\rho_\infty, 0, 0, u_0, p_\infty) + \chi u_0(0, \epsilon_1, \epsilon_2, \epsilon_3, 0) & |r| < d_0/2, \\ (\rho_\infty, 0, 0, 0, p_\infty) & |r| \geqslant d_0/2. \end{cases} \tag{2.18}$$

Here, χ is a scaling factor and set to be 1.0×10^{-2}. The initial condition for grid B is prepared by interpolating the resulting flow fields of grid A. After the flow field reaches equilibrium, physical quantities are sampled for approximately $1.75 \times 10^4 L_{im}/c_\infty$ for grid A and $478 L_{im}/c_\infty$ for grid B.

3. Periodicity of the computed phenomena and validation of the present computation

Periodicity of the computed phenomena is checked by the time histories of pressure variation at $(r, z) = \text{P1} : (d_0/2, L_{im}/2)$, i.e. near the middle of the jet shear layers, and $\text{P2} : (1.82d_0, L_{im}/2)$, i.e. far from the jet, the mass flow variation through the hole, the space–time plots of pressure fluctuation, and the radial and streamwise velocities around the hole, the latter two of which are mentioned later in §§ 4.2 and 6, respectively. Figure 6(*a*,*b*) shows the time histories of pressure variation at P1 and P2. The abscissa $0 \leqslant t_g^* \leqslant t_{gmax}^* = 927.4$ is the time from the initial condition non-dimensionalized by L_{im} and c_∞. The ordinate is the pressure variation $p''(t)$ around the average of whole data, i.e.

$$p''(t) = p(t) - \overline{p}, \quad \overline{p} \equiv \int_0^{t_{gmax}^*} p(t)\,\mathrm{d}t. \tag{3.1}$$

In the figures, transient non-periodic pressure variation is observed for $0 \leqslant t_g^* < 330$, and the variation starts to become periodic at $t_g^* \sim 330$; $t^* = 0$ and $t = 0$, which appear in figures 7, 10–17, 19 and 21–24, correspond to $t_g^* = 567$ and $t^* = 2.16$, respectively. Figure 7 shows the time histories of the non-dimensional mass flow rates $\dot{m}_h^\dagger$ at the

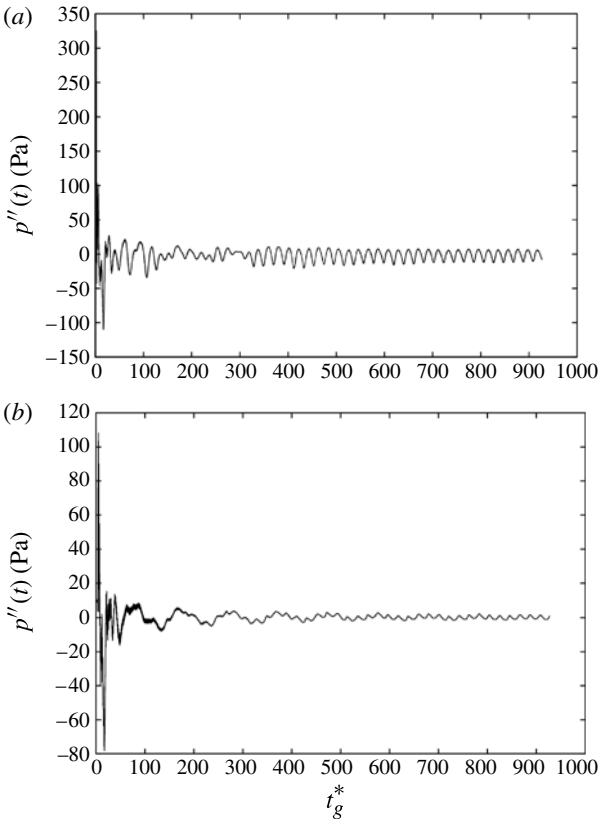

FIGURE 6. Time histories of pressure variation at (*a*) $(r, z) = \text{P1}: (d_0/2, L_{im}/2)$ (near the middle of the jet shear layer) and (*b*) $(r, z) = \text{P2}: (1.82d_0, L_{im}/2)$ (far from the jet).

inlet of the end plate hole, i.e. $z = 50$ mm. $\dot{m}_h^\dagger$ is defined by

$$\dot{m}_h^\dagger \equiv \frac{\dot{m}_h}{\pi\,(d_0/2)^2\,\rho_\infty u_0}, \tag{3.2}$$

and the mass flow rates $\dot{m}_h$ are evaluated as

$$\dot{m}_h \equiv \int_\Omega \rho u_z \,\mathrm{d}r\,\mathrm{d}\theta, \quad \Omega \equiv \{(r,\theta);\,(r,\theta) \in [0, d_0/2] \times [0, 2\pi)\}. \tag{3.3}$$

The variation of the mass flow rates is also periodic, corresponding to the periodic pressure variation. The periodicity of the computed results is also confirmed by the radial and streamwise velocities around the hole in figure 22, which will be referred to later.

Figure 8 shows a comparison of the sound pressure levels (SPL) between the computations and the experiment for $u_0 = 10$ m s^{-1}. For the estimation of SPL in the computation, the time series data of pressure variation between $449 \leqslant t_g^* \leqslant 927$ shown in figure 6 are employed. The sound pressure levels are evaluated at both P1 and P2. The most dominant hole tone peak frequencies are 330 Hz for the computation and 320 Hz for the experiment, and therefore the most dominant experimental frequency is

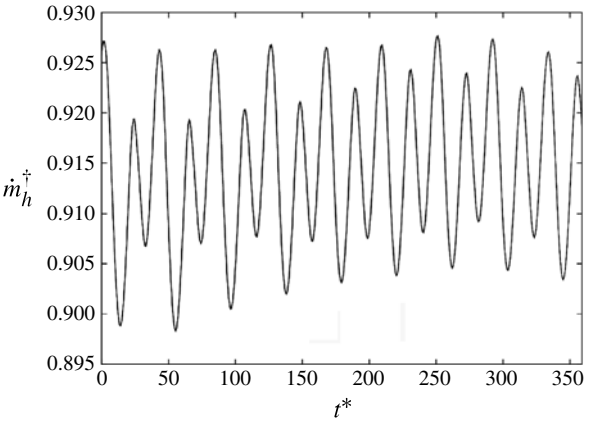

FIGURE 7. Time variation of mass flow through the end plate hole.

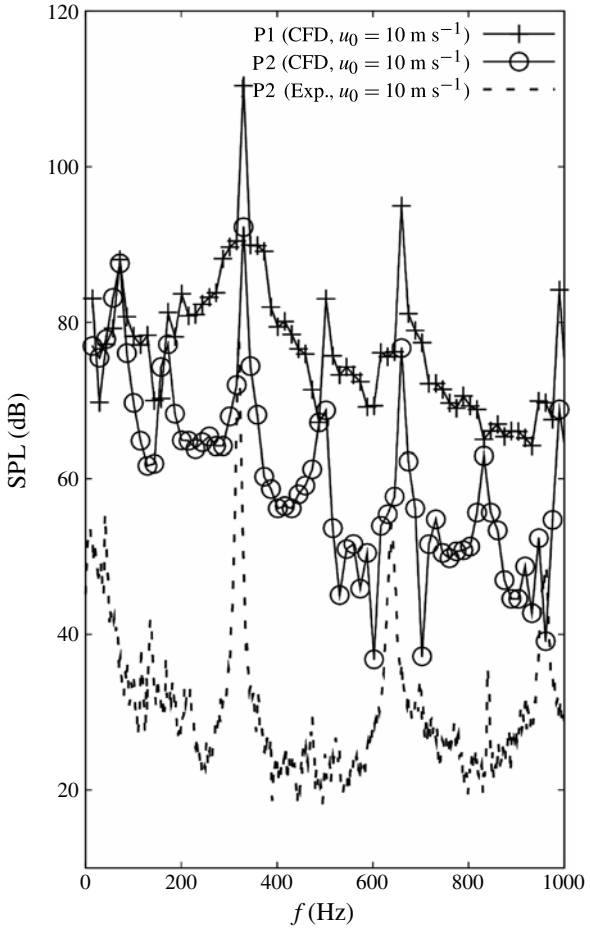

FIGURE 8. Comparison of sound pressure levels between the computations and experiment for $u_0 = 10$ m s^{-1}: P1, $(d_0/2, L_{im}/2)$; P2, $(1.82d_0, L_{im}/2)$.

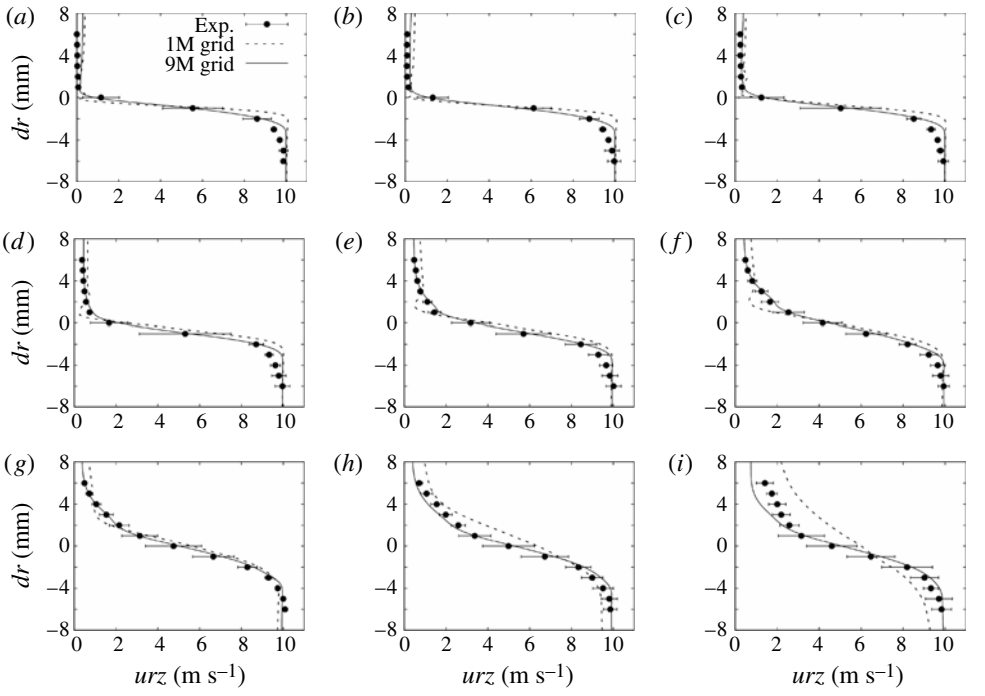

FIGURE 9. Comparison of the distribution of non-circumferential velocity magnitude $\sqrt{u_r^2 + u_z^2}$ around $r = d_0/2$ between the experiment and the computation with the 1M and 9M grids ($urz \equiv \sqrt{u_r^2 + u_z^2}$ and $dr \equiv r - r_0$, $r_0 \equiv d_0/2$): (*a*) $z = 5$ mm, (*b*) $z = 10$ mm, (*c*) $z = 15$ mm, (*d*) $z = 20$ mm, (*e*) $z = 25$ mm, (*f*) $z = 30$ mm, (*g*) $z = 35$ mm, (*h*) $z = 40$ mm, (*i*) $z = 45$ mm.

accurately predicted by the computation, while the difference in the magnitude of the sound pressure levels is ∼14 dB. When a room temperature variation of ±1 °C and the uncertainties in the inlet disturbances are taken into account, the above difference is considered to be small.

The most dominant peak frequency $f \sim 330$ Hz at P1 is the same as that at P2. Therefore, flow fields in this hole tone system, which include not only the immediate neighbourhood of the jet but also regions far away from the jet, are judged to have reached a periodic equilibrium state. The frequency of the periodic variation of the pressure at both P1 and P2 and that of the mass flow rates are the same as the most dominant hole tone frequency, as shown later in figure 22.

In figure 9, comparisons are shown for the radial distribution of non-circumferential velocity magnitude $\sqrt{u_r^2 + u_z^2}$ around $r = 25.5$ mm between the experiments and the computations with the 1M and 9M grids. The experimental data are shown in the range $dr = -6$ to 6 mm, where $dr \equiv r - r_0$, $r_0 = d_0/2$ when $u_0 = 10$ m s^{-1}. The measurements were conducted three times. The black points and error bars in the figure show the averages $\bar{x}$ and the 90 % confidence intervals

$$\left[\bar{x} - t_{N_{max}-1}\frac{\sigma}{\sqrt{N_{max}}}, \bar{x} + t_{N_{max}-1}\frac{\sigma}{\sqrt{N_{max}}}\right]. \tag{3.4}$$

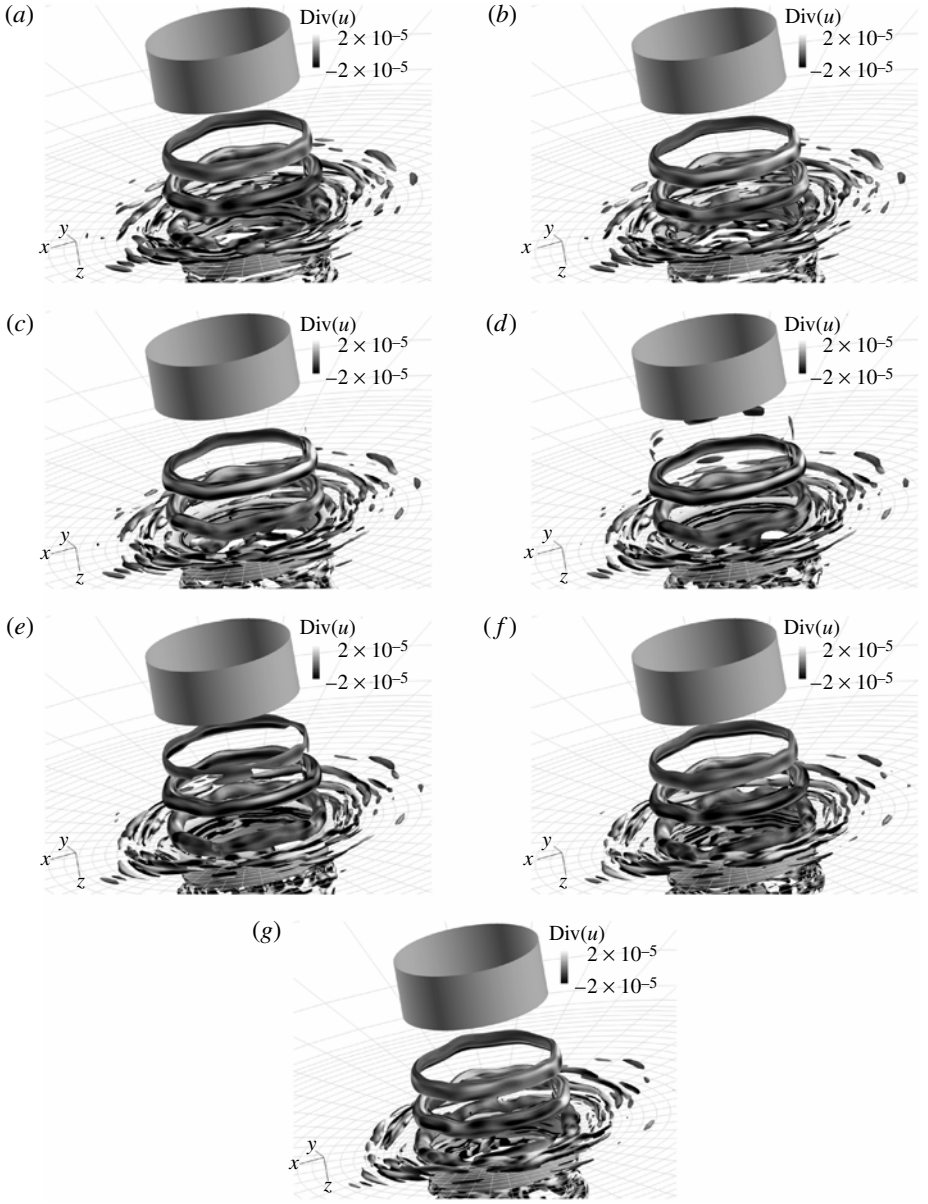

FIGURE 10. Visualization of vortical structures by the iso-surfaces of the second invariant of the velocity gradient tensor $Q^{\dagger} = 14.5$ ($1/T_f \sim 330$ Hz). Times: (*a*) $t = 0$, (*b*) $t = T_f/6$, (*c*) $t = 2T_f/6$, (*d*) $t = 3T_f/6$, (*e*) $t = 4T_f/6$, (*f*) $t = 5T_f/6$, (*g*) $t = 6T_f/6$.

Here,

$$N_{max} = 3, \quad \bar{x} \equiv \frac{1}{N_{max}} \sum_{i=1}^{N_{max}} x_i, \quad \sigma \equiv \sqrt{\frac{1}{N_{max} - 1} \sum_{i=1}^{N_{max}} (x_i - \bar{x})^2}, \tag{3.5}$$

and $t_{N_{max}-1} = 2.920$ for Student's t-distribution (Student 1908). Initially thin shear layers near the nozzle exit $z \sim 5$ mm gradually become thick in the latter half of the L_{im} as the disturbances around the jet develop, which is seen in figure 5 of Matsuura & Nakano (2011). In the computations with the 1M grid, the jet shear layers are diffused compared with the experimental data around $z = 40$ to 45 mm. While some deviations are observed also for $dr \sim -3$ mm of $z = 0$ to 20 mm, and $dr > 3$ mm of $z = 45$ mm, the computation with the 9M grid much improves the diffusion mentioned above and predicts the downstream variation of the velocity profiles very well.

Figure 10 shows vortical structures visualized by the iso-surfaces of the second invariant of the velocity gradient tensor $Q^\dagger = 14.5$ for a period T_f. Here, $Q^\dagger$ is defined by

$$Q^\dagger = \tfrac{1}{2}(-S^\dagger_{ij}S^\dagger_{ji} + \Omega^\dagger_{ij}\Omega^\dagger_{ij}), \tag{3.6}$$

where $S^\dagger_{ij}$ is the rate of strain tensor and $\Omega^\dagger_{ij}$ is the vorticity tensor. $Q^\dagger$, $S^\dagger_{ij}$, $\Omega^\dagger_{ij}$ are non-dimensionalized by u_0 and L_{im}. Vortex rings formed in the jet shear layer are observed in figure 10. The vortex rings convect downstream, and impinge on the hole edge. A new vortex ring is generated upstream near the nozzle exit, and the process is repeated accompanying the periodic variation of pressure and the mass flow rates mentioned in figures 6 and 7. Although the vortex rings visualized in figure 10 are approximately axisymmetric, some azimuthal deformation of the vortex rings is also visible. However, the asymmetry is much less apparent in the pressure fluctuation fields in figure 13, and therefore we neglect the effects of the inhomogeneity in the azimuthal direction.

In summary, these computations agree reasonably well with experiment.

4. Vortex impingement and pressure wave propagation

4.1. *The relationship between pressure distribution of shear layers, velocity vectors and separation at the edge*

To clarify the details of the hole tone feedback mechanism, we first investigated the vortex impingement processes. Figure 11 shows the time variation of pressure fluctuation Δp and velocity fields due to shear-layer impingement on the hole edge where $\Delta p = p - p_\infty$ and $p_\infty = 101,325$ Pa. Figure 12 shows a magnified view of figure 11 in the neighbourhood of the hole edge. Regions of $\Delta p < 0$ are shown by dashed lines and those of $\Delta p \geqslant 0$ by solid lines. The labels $a_1, \ldots, k_1$ are used in figure 11 and $a_2, \ldots, l_2$ are used in figure 12.

Successive high and low pressure regions are formed in the jet shear layers. The low pressure regions contain backflows that cause entrainment of the surrounding fluids into the jets, and therefore correspond to vortices. The high pressure regions are formed between the vortices. A simple explanation for the formation of the high pressure regions is given in appendix A.

At $t = 0$, a low pressure region a_1 is going to get into the hole near the hole edge; a small vortex a_2 which facilitates fluid entrainment to the hole is also observed on the upstream surface of the hole edge. The small separation region b_2 originally generated at the upstream edge of the hole on previous occasions is observed on the interior surface of the hole. Slightly away from the edge on the upstream side of the end plate, a low pressure region b_1 is observed.

At $t = T_f/6$, the large high pressure region c_1 is formed on the upstream side of the edge, and the low pressure region d_1 is formed on the interior side of the edge. Velocity vectors c_2 around $(r, z) = (d_0/2, L_{im})$ slightly point to the lower right. As a

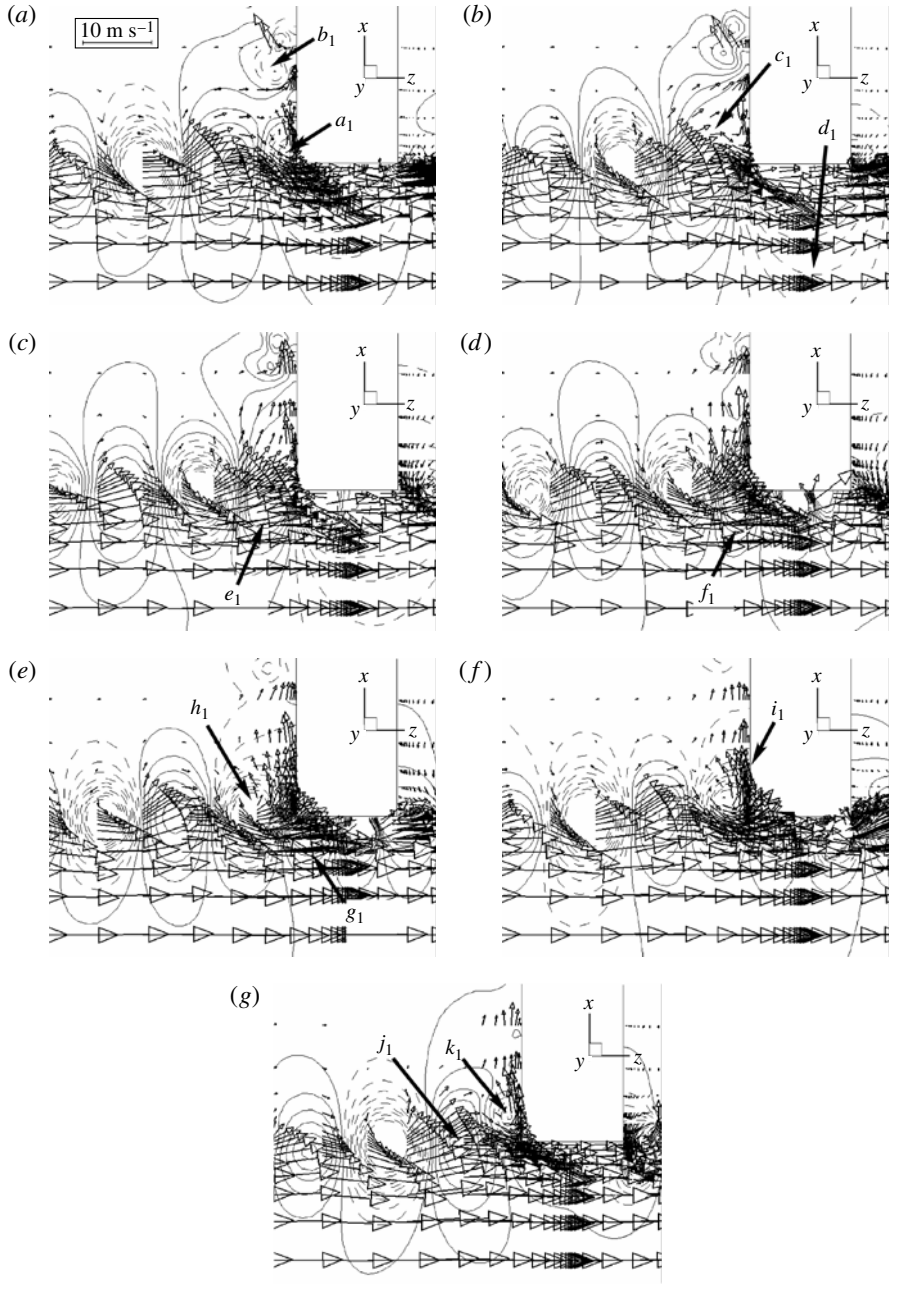

FIGURE 11. Time variation of pressure fluctuation Δp and velocity fields due to shear-layer impingement on the hole edge ($1/T_f \sim 330$ Hz). Solid lines, positive Δp; dashed lines, negative Δp. Times: (*a*) $t = 0$, (*b*) $t = T_f/6$, (*c*) $t = 2T_f/6$, (*d*) $t = 3T_f/6$, (*e*) $t = 4T_f/6$, (*f*) $t = 5T_f/6$, (*g*) $t = 6T_f/6$.

result, the inception of separation d_2 takes place near the upstream edge of the hole. Near the downstream edge of the hole, a vortex starts to leave from the edge.

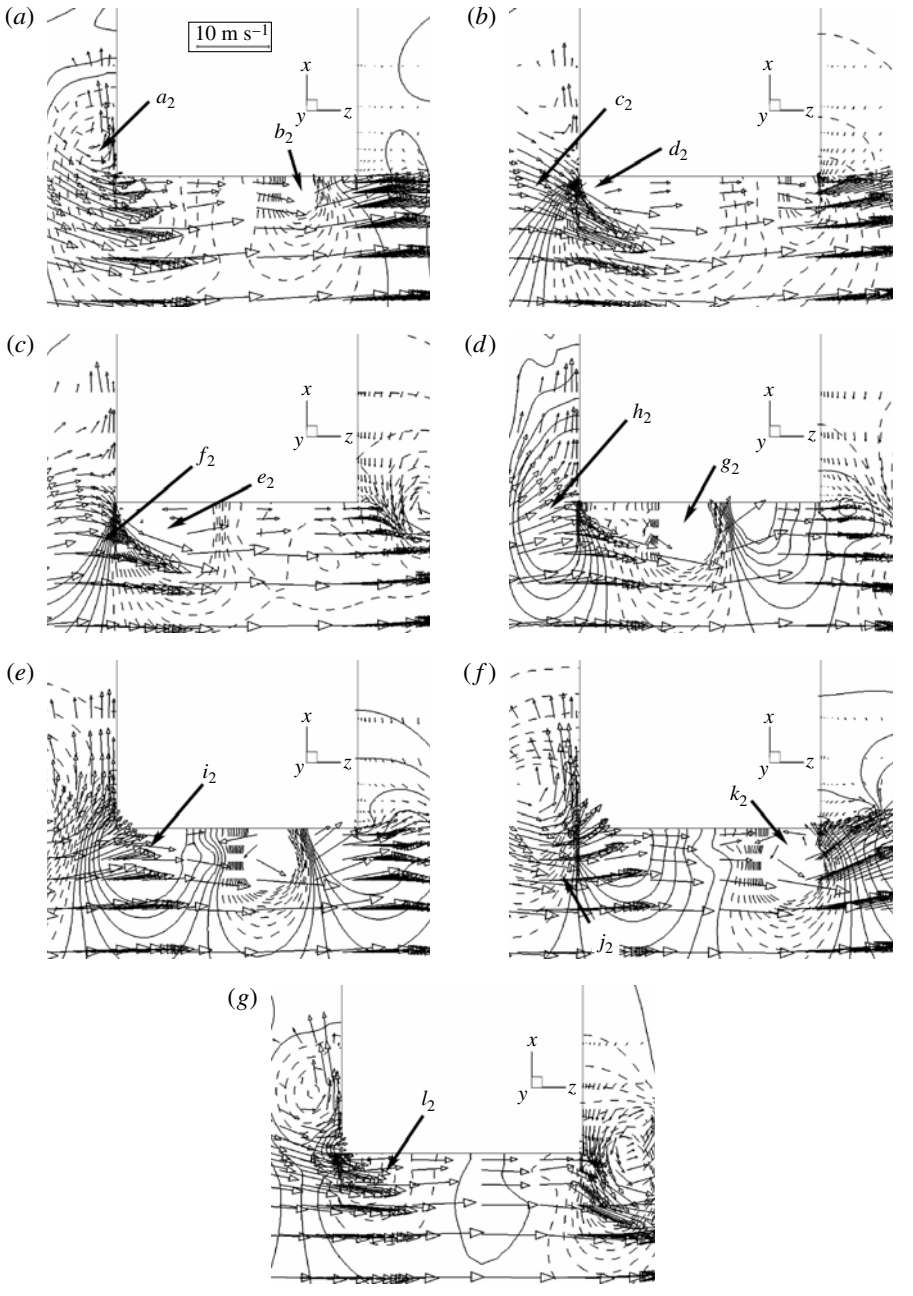

FIGURE 12. Time variation of pressure fluctuation Δp and velocity fields due to shear-layer impingement on the hole edge in the neighbourhood of the edge ($1/T_f \sim 330$ Hz). Solid lines, positive Δp; dashed lines, negative Δp. Times: (*a*) $t = 0$, (*b*) $t = T_f/6$, (*c*) $t = 2T_f/6$, (*d*) $t = 3T_f/6$, (*e*) $t = 4T_f/6$, (*f*) $t = 5T_f/6$, (*g*) $t = 6T_f/6$.

At $t = 2T_f/6$, the high pressure region c_1 observed on the upstream side of the edge now diminishes as e_1. From figure 12(*c*) the separation region e_2 grows on the interior side of the edge, while the velocity vectors f_2 at $z \sim 50$ mm are almost in

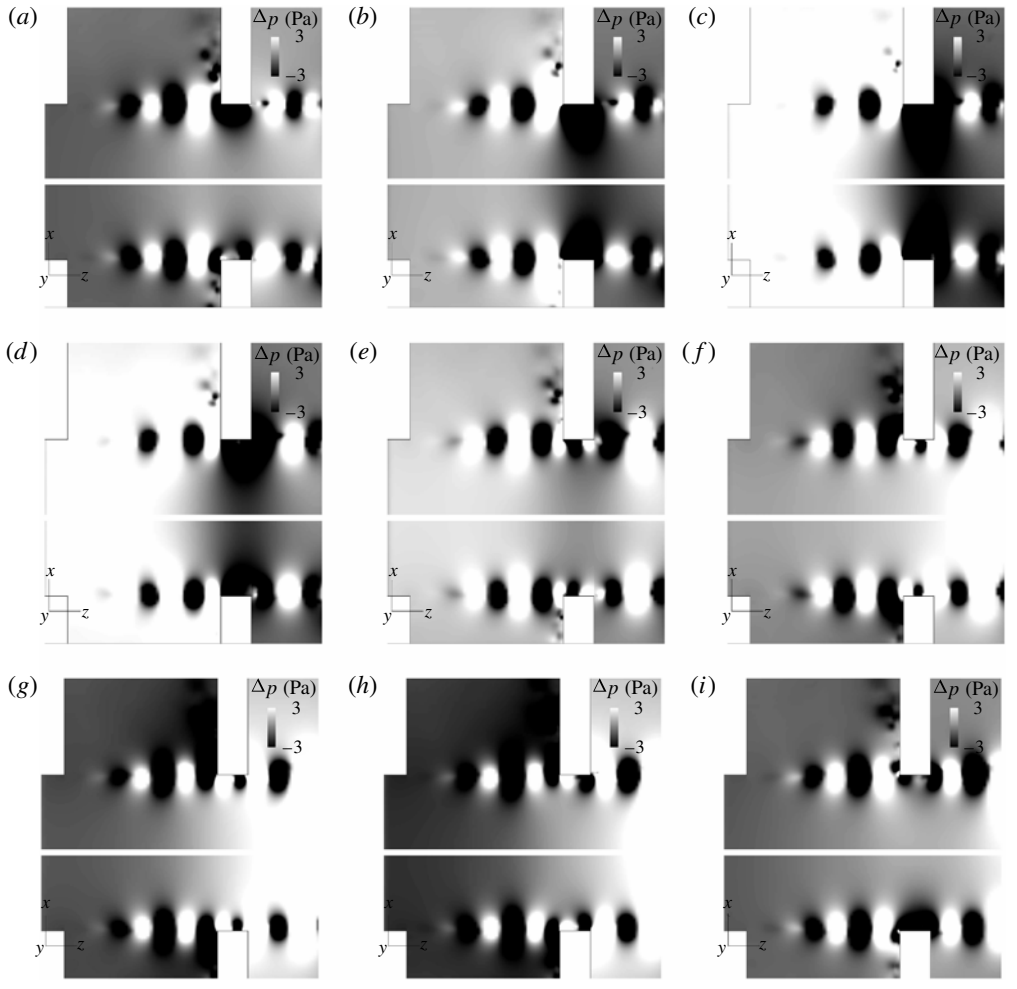

FIGURE 13. Time variation of pressure fluctuation distribution Δp Pa upstream and downstream of the end plate ($1/T_f \sim 330$ Hz). Times: (*a*) $t = 0$, (*b*) $t = T_f/8$, (*c*) $t = 2T_f/8$, (*d*) $t = 3T_f/8$, (*e*) $t = 4T_f/8$, (*f*) $t = 5T_f/8$, (*g*) $t = 6T_f/8$, (*h*) $t = 7T_f/8$, (*i*) $t = 8T_f/8$.

the $+z$ direction. The vortex near the downstream edge of the hole leaves the edge slightly downstream.

At $t = 3T_f/6$, the high pressure region f_1 in figure 11(*d*) on the upstream side of the edge becomes much smaller compared with e_1 in figure 11(*c*). In figure 12(*d*), velocity vectors h_2 point to the upper right in the high pressure region slightly upstream of the hole inlet. The separation region e_2 observed near the edge in figure 12(*c*) is convected downstream as g_2 to the middle of the hole.

At $t = 4T_f/6$, the high pressure region f_1 observed near the edge in figure 11(*d*) starts to get into the hole as g_1. Velocity vectors point to the upper right as found in i_2 in figure 12(*e*). Separation near the interior side of the upstream edge observed in figure 12(*b–d*) almost disappears, and the attached boundary layers grow in conjunction with the high pressure region near the upstream side of the edge. The separation region g_2 observed in figure 12(*d*) approaches the hole edge. The vortex h_1

with backflow is observed a little away from the upstream surface of the end plate in figure 11(*e*).

At $t = 5T_f/6$, the low pressure region h_1 observed in figure 11(*e*) now impinges on the hole edge. Because of the vorticity of the low pressure region near the upstream side of the hole edge, velocity vectors i_1 near the upstream side of the end plate turn upstream, i.e. the $-z$ direction. In figure 12(*f*), velocity vectors j_2 between the high pressure region and the low pressure region point upward much more than in figure 12(*e*), and the $+z$ directional component of the velocity vectors decrease, consequently alleviating the high pressure near the edge. The separation region k_2 that originally formed around $t \sim 2T_f/6$ is now on the edge of the exit side of the hole.

At $t = 6T_f/6$, the high pressure region near the edge observed in figure 12(*f*) disappears, and another high pressure region j_1 approaches the hole edge. Two weak low pressure regions k_1 and l_2 are distributed on both the upstream and interior side of the hole. Compared with figure 11(*a*), the low pressure region k_1 on the upstream side of the edge proceeds in a radial direction. No evident separation is observed inside the hole, and an attached boundary layer with a weak pressure gradient develops near the interior side of the edge.

4.2. *Pressure wave propagation*

Here, we clarify the global propagation of pressure waves due to vortex impingement. Figure 13 shows the time variation of the pressure fluctuation Δp distribution upstream and downstream of the end plate. The region outside the range $-3 \leqslant \Delta p \leqslant 3$ is excluded in order to emphasize the relative ambient pressure distribution between the space upstream and downstream of the end plate. In addition to the periodic pressure distribution in the jet shear layers, high and low ambient pressure regions alternately appear over a wide area upstream and downstream of the end plate, and the hole part becomes a node for the change. Pressure waves pass through the jet, and the jet including its shear layers oscillates periodically. For times $t = 0$ to $2T_f/8$, the ambient pressure upstream of the end plate gradually increases, and the ambient pressure downstream of the end plate gradually decreases. For $t = 3T_f/8$ to $6T_f/8$, the ambient pressure upstream of the end plate gradually decreases, and the ambient pressure downstream of the end plate gradually increases. For $t = 7T_f/8$ to $8T_f/8$, the ambient pressure upstream of the end plate gradually increases again, and the ambient pressure downstream of the end plate gradually decreases again. Here, we look at the relationship between the ambient pressures and the pressure distribution around the hole edge. When high pressure regions impinge on the upstream surface of the hole edge, the ambient pressure upstream of the end plate becomes high. At the same time, low pressure regions are formed on the downstream surface of the hole edge as well as the low ambient pressure region downstream of the end plate. When low pressure regions impinge on the upstream surface of the hole edge, the ambient pressure upstream of the end plate becomes low. At the same time, high pressure regions are formed on the downstream surface of the hole edge as well as the high ambient pressure region downstream of the end plate.

Figure 14 shows the detailed propagation of pressure waves due to the impingement of the high pressure region on the hole edge for times $t = 0.116T_f$ to $0.156T_f$. Time increments Δt_{inc} are $\Delta t_{inc} \sim 0.006T_f$ for (*a–f*), and $\Delta t_{inc} = 0.003T_f$ for (*g–i*). First, compression waves propagate upstream outside the jet, and increase the pressure there, as shown by arrows in figure 14(*a–f*). Then, the pressure inside the jet also increases to the same pressure level as outside the jet due to the upstream propagation of compression waves, as shown by arrows in figure 14(*g–i*).

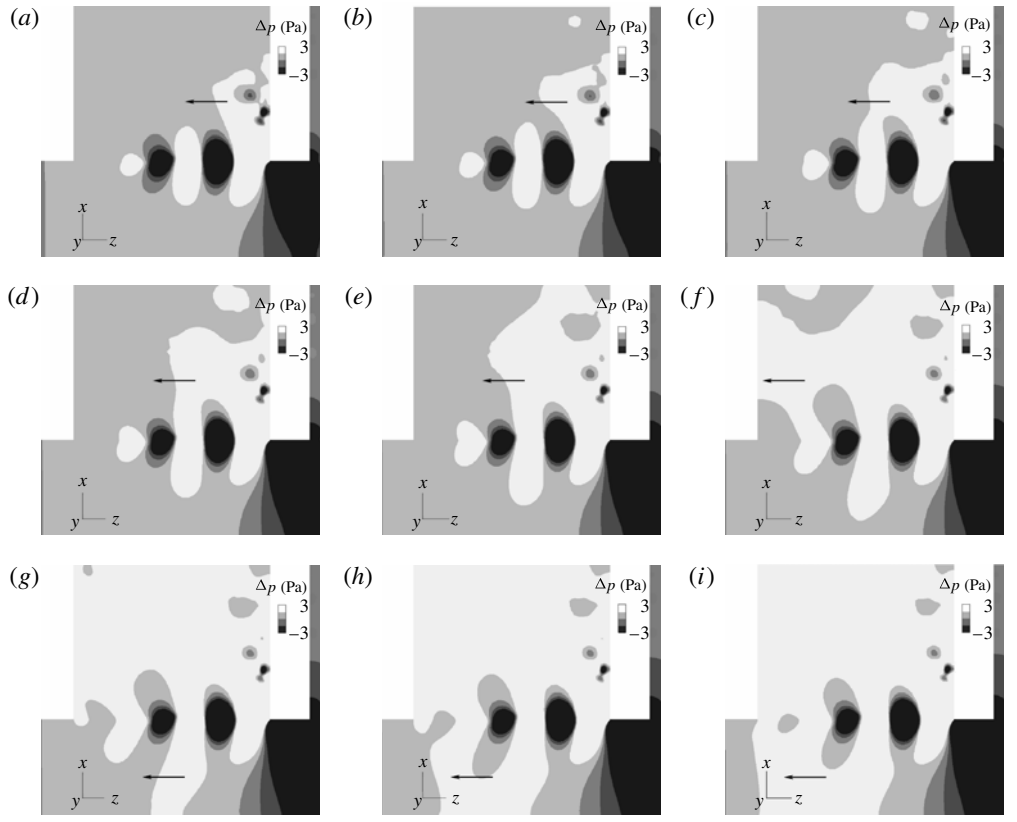

FIGURE 14. Detailed propagation of pressure waves due to the impingement of the high pressure region on the hole edge for times $t = 0.116T_f$ to $0.156T_f$. Δp Pa is shown. Time increments in (*a–f*) are different from those in (*g–i*). Times: (*a*) $t = 0.116T_f$, (*b*) $t = 0.122T_f$, (*c*) $t = 0.128T_f$, (*d*) $t = 0.134T_f$, (*e*) $t = 0.141T_f$, (*f*) $t = 0.147T_f$, (*g*) $t = 0.150T_f$, (*h*) $t = 0.153T_f$, (*i*) $t = 0.156T_f$.

Figure 15 shows the detailed propagation of pressure waves due to the impingement of the low pressure region on the hole edge for times $t = 0.659T_f$ to $0.762T_f$. Time increments Δt_{inc} are $\Delta t_{inc} \sim 0.016T_f$ for (*a–f*), and $\Delta t_{inc} = 0.009T_f$ for (*g–i*). First, expansion waves propagate upstream outside the jet, and decrease the pressure there as shown by arrows in figure 15(*a–f*). After the pressure outside the jet decreases, pressure inside the jet also decreases from upstream, as shown by arrows in figure 15(*e–i*). In this way, a back-and-forth phenomenon, which does not occur in the propagation of the compression waves, occurs in the propagation of the expansion waves. Therefore, the directions of the pressure wave propagation are different between the compression process and the expansion process. Figure 16 shows space–time plots, i.e. the time evolution of the pressure fluctuation distribution at $r = 5, 20, 40, 94$ mm. Here, $r = 5$ mm corresponds to the neighbourhood of the centreline, $r = 20$ mm corresponds to the jet shear layer, and $r = 40$ and 94 mm correspond to the outside of the hole. The ordinate is the non-dimensional time t^* and the abscissa is the z coordinate, where $z = 0$ mm corresponds to the nozzle exit as explained in § 2.2. The times $t = 0, T_f$ in figures 10–13 correspond to the

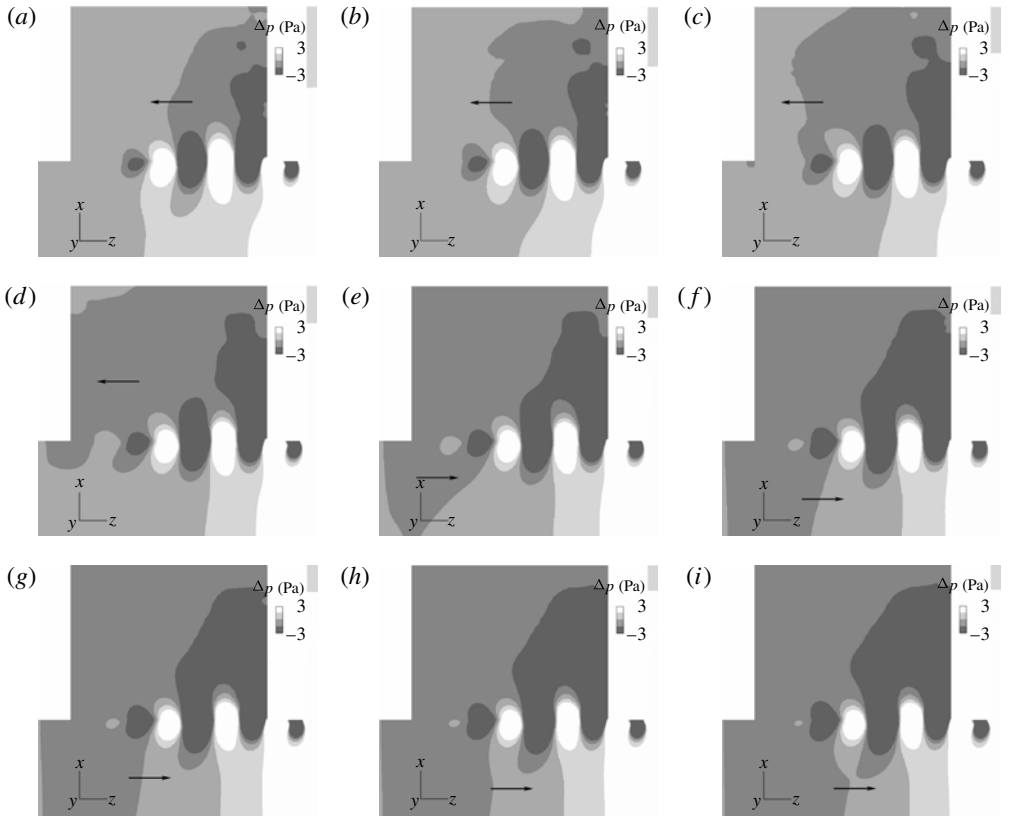

FIGURE 15. Detailed propagation of pressure waves due to the impingement of the low pressure region on the hole edge for times $t = 0.659T_f$ to $0.762T_f$. Δp Pa is shown. Time increments in (*a–f*) are different from those in (*g–i*). Times: (*a*) $t = 0.659T_f$, (*b*) $t = 0.675T_f$, (*c*) $t = 0.691T_f$, (*d*) $t = 0.706T_f$, (*e*) $t = 0.722T_f$, (*f*) $t = 0.738T_f$, (*g*) $t = 0.744T_f$, (*h*) $t = 0.753T_f$, (*i*) $t = 0.762T_f$.

times $t^* = 2.16, 25.2$ respectively, as shown in figure 16. For comparison, the sound speed propagation from downstream to upstream and from upstream to downstream is shown by the arrow with c_∞. The arrow with c_∞ does not necessarily mean that the apparent pressure waves propagate upstream, or downstream, at the speed of sound because Δp is not a purely acoustic pressure. The apparent propagation speeds also depend on the selection of Δp.

At $r = 5$ mm, a low pressure region 'A' is formed inside and downstream of the end plate hole, and a high pressure region 'B' is formed just upstream of the end plate hole. Pressure waves propagate upstream for the formation of region 'B' as found by the inclination of the contours below it. A high pressure region 'C' is then formed inside and downstream of the end plate hole, a low pressure region 'D' is formed near the nozzle exit, and pressure waves propagate downstream for the formation of region 'D'. When figure 16(*a*) is compared with figure 13, regions 'A' and 'B' approximately correspond to the pressure distribution of figure 13(*c*,*d*). Region 'C' in figure 16(*a*) corresponds to the high pressure regions in figure 13(*f*,*g*) downstream of the hole, and region 'D' in figure 16(*a*) corresponds to the low pressure region in figure 13(*h*). At $r = 20$ mm, the high and low pressure regions convect downstream slowly with the

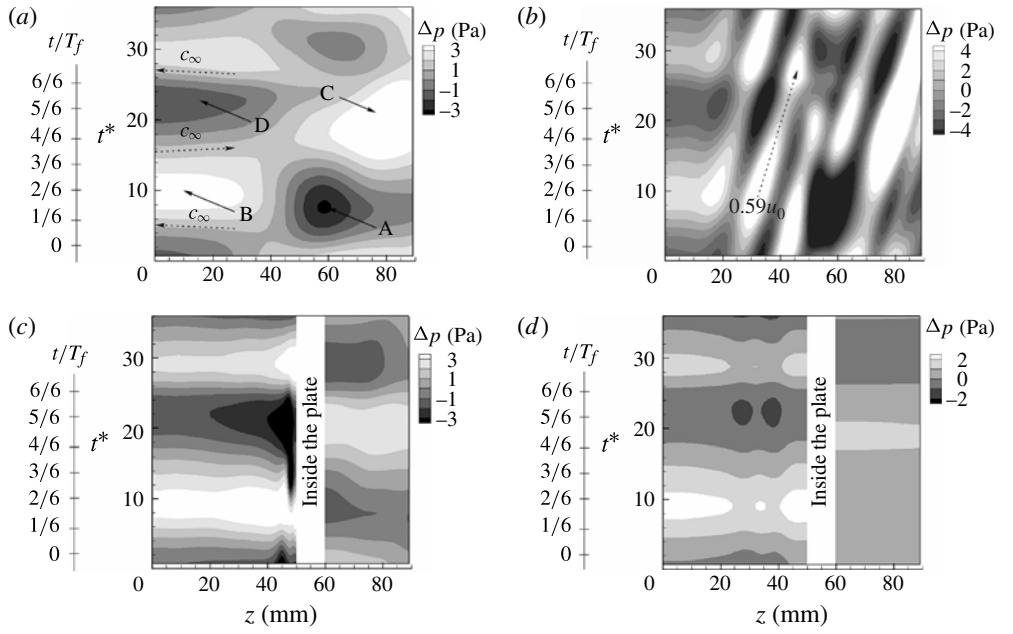

FIGURE 16. Space–time plots of pressure fluctuation Δp at $r = 5, 20, 40, 94$ mm ($z = 0$, nozzle exit): (*a*) $r = 5$ mm (near the centreline); (*b*) $r = 20$ mm (near the jet shear layer); (*c*) $r = 40$ mm (outside the hole, close to the centreline); (*d*) $r = 94$ mm (outside the hole, far from the centreline).

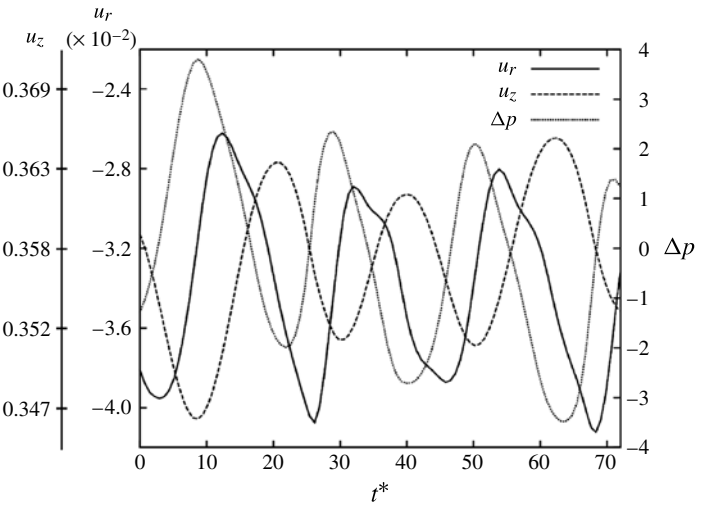

FIGURE 17. Time histories of u_r m s^{-1}, u_z m s^{-1} and Δp Pa near the nozzle exit, i.e. $(r, z) = (25.5$ mm, 0.54 mm).

convection velocity of approximately $0.59u_0$. At $r = 40$ and 94 mm, which is outside the jet, the variation of Δp in the z direction becomes small. From the pressure signals

between $z = 20$ and 30 mm at $r = 40$ mm, the speed of the pressure wave propagation is estimated to be larger than $\sim 0.85 c_\infty$.

With figures 13–16 taken into account, dominant pressure fluctuations in this feedback system propagate both inside and outside the jet with the alternate appearance of the wide high and low pressure regions upstream and downstream of the end plate hole, and the frequencies of the pressure fluctuations and vortices in the shear layer coincide. It has been thought for some time that pressure waves outside the jet trigger the feedback of the hole tone regarding the feedback mechanism mentioned in § 1. The global phenomena explained above are newly discovered feedback phenomena (Matsuura & Nakano 2011).

Figure 17 shows the time histories of u_r, u_z and Δp near the nozzle exit, i.e. $(r, z) = (25.5 \text{ mm}, 0.54 \text{ mm})$. The phases of u_z and Δp are opposite, which means that compression, i.e. a high Δp, decreases u_z, and expansion, i.e. a low Δp, increases u_z; u_r, which is a disturbance leading to the large vortices in the jet shear layer, is generated with a phase advance of $\pi/2$ rad compared to u_z.

These feedback phenomena consist of four elements, i.e. the birth of disturbances in the jet shear layer, the convection and amplification of the disturbances leading to the formation of vortices, the generation of pressure waves due to vortex impingement, and the upstream propagation of pressure waves which initiate the disturbances. It might be important to maintain the feedback loop that the vortex impingement, associated with the alternative global fluctuations of the background pressures between the upstream and downstream sides of the end plate, generates the periodic fluctuation of pressure waves near the upstream edge of the end plate hole, which are propagating upstream both inside and outside the jet. While the former two elements observed in this paper do not alter existing views (Rayleigh 1945; Chanaud & Powell 1965), new aspects of the mutual relationship between the latter two elements are given in the feedback process mentioned above (Matsuura & Nakano 2011).

5. Proper orthogonal decomposition analysis for the relationship between the pressure field and mass flow rate through the hole

In § 4.1 and appendix A, it is found that the distribution of pressure fluctuations in the jet shear layers represents that of vortical structures. On the other hand, the timing of the global propagation of pressure waves is closely related to the vortex impingement and the associated distribution of vortical structures around the end plate hole.

Here, to extract dominant unsteady behaviours, which are mutually independent, of the hole tone phenomenon, a POD analysis is performed. The method used in this study is Sirovich's snapshot POD method (Sirovich & Rodriguez 1987). By using this method, the whole pressure fluctuation field on $\Omega_{all} \equiv \bigcup_{k=1}^{N_d} \Omega_k$ is orthogonally decomposed based on M instantaneous snapshots of the whole flow field. Here, Ω_k, $k = 1, \ldots, N_d$ corresponds to each zone mentioned in § 2.2, and N_d is the total number of the zones, i.e. $N_d = 5$. In the method, fluctuation $p'(x, t) = p(x, t) - \overline{p(x)}$ is expanded by a set of eigenfunctions $\{\phi_i(x)\}_{i=1}^M$, which are also called 'modes', and the corresponding coefficients $\{a_i(t)\}_{i=1}^M$ as

$$p'(x, t) \sim p'_M(x, t) \equiv \sum_{i=1}^{M} a_i(t)\phi_i(x), \quad (t, x) \in I \times \Omega_{all}. \tag{5.1}$$

Here, $\overline{p(x)}$ is the time-averaged pressure field. $\overline{p(x)}, p'(x,\cdot), p'_M(x,\cdot)$ and $\phi_i(x)$ are all N_{all}-dimensional vectors of positions with a single coordinate. I is a set of times where snapshots are sampled. N_{all} is the total number of grid points in Ω_{all}, that is,

$$N_{all} \equiv \sum_{k=1}^{N_d} N_k. \tag{5.2}$$

Here, N_k is the number of grid points in Ω_k. Strictly speaking, there is duplication of elements in $p'(x,\cdot)$ because $\exists i,j \in \{1,\ldots,N_d\}$ of $i \neq j$, $\Omega_i \cap \Omega_j \neq \phi$. However, the measures of $\Omega_i \cap \Omega_j$ for such i,j are very small compared with those of the zones, and therefore the duplication is considered to be negligible in these analyses. As discussed later on, the eigenfunctions $\{\phi_i(x)\}_{i=1}^M$ and the corresponding coefficients $\{a_i(t)\}_{i=1}^M$ are successfully evaluated by this treatment. In this study, the snapshots are collected every $3000\Delta t$. M is varied as 100, 200 and 300, and $M = 200$ is used finally, based on the discussion of the statistical convergence of the eigenvalues described later.

The eigenfunctions $\phi_i(x)$ are obtained by the algebraic equation

$$\boldsymbol{C} f_i = \lambda_i f_i. \tag{5.3}$$

Here, $\boldsymbol{C} = (C_{m,n})$ is an $M \times M$ matrix, λ_i is an eigenvalue, and $f_i = (f_{m,i})$ is an eigenvector. The elements $C_{m,n}$ are defined by

$$C_{m,n} \equiv \langle p'(x,t_m), p'(x,t_n)\rangle, \quad m,n \in \{1,\ldots,M\}, \tag{5.4}$$

where $\langle\cdot,\cdot\rangle$ is the Euclidean inner product. The above eigenvectors are scaled such that

$$\|f_i\|^2 = \sum_{k=1}^{M} f_{k,i}^2 = \lambda_i, \quad i \in \{1,\ldots,M\}. \tag{5.5}$$

Then, the eigenfunction $\phi_i(x)$ is defined by

$$\phi_i(x) \equiv \frac{1}{\lambda_i} \sum_{k=1}^{M} f_{k,i} p'(x,t_k). \tag{5.6}$$

The eigenfunction $\phi_i(x)$ has a property such that

$$\phi_k(x) \cdot \phi_l(x) = \delta_{kl}, \quad k,l \in \{1,\ldots,M\}, \tag{5.7}$$

where δ_{kl} is Kronecker's delta function. Using the orthogonality of $\phi_i(x)$, the coefficient $a_i(t)$ is derived as

$$a_i(t) = \phi_i(x) \cdot p'(x,t)^t. \tag{5.8}$$

Figure 18 shows the fractional energies of the first 20 dominant POD modes for $M = 100, 200$ and 300. Irrespective of the values of M, the most dominant mode occupies nearly 47 % of the total energy, and the second dominant mode occupies nearly 23 %. While there is a small difference between the results of $M = 100$ and 200, the difference between the results of $M = 200$ and 300 is negligible for the two dominant modes. Therefore, $M = 200$ is used for the later discussion.

Figure 19 shows the time histories of the pressure fluctuation, i.e. $p'(t)$, the reconstructed pressure fluctuation from the dominant 20 POD modes, i.e. $P'_{20}(x,t)$, the first POD mode, i.e. $a_1(t)\phi_1(x)$, and the second POD mode, i.e. $a_2(t)\phi_2(x)$, at $(r,z) = (d_0/2, 0.964L_{im})$ and $(d_0/2, 1.238L_{im})$. The reconstructed pressure fluctuation from the dominant 20 POD modes reproduces the original pressure fluctuation

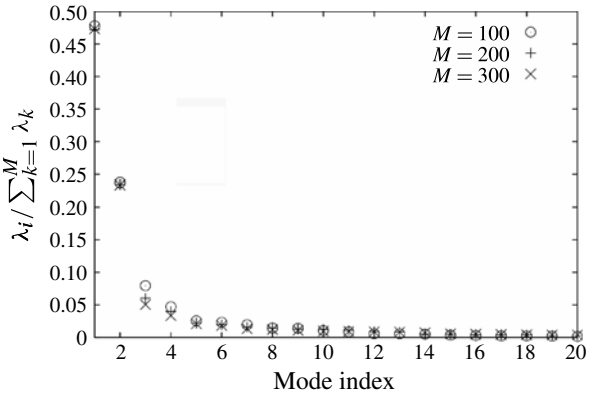

FIGURE 18. Fractional energies of the first 20 dominant POD modes.

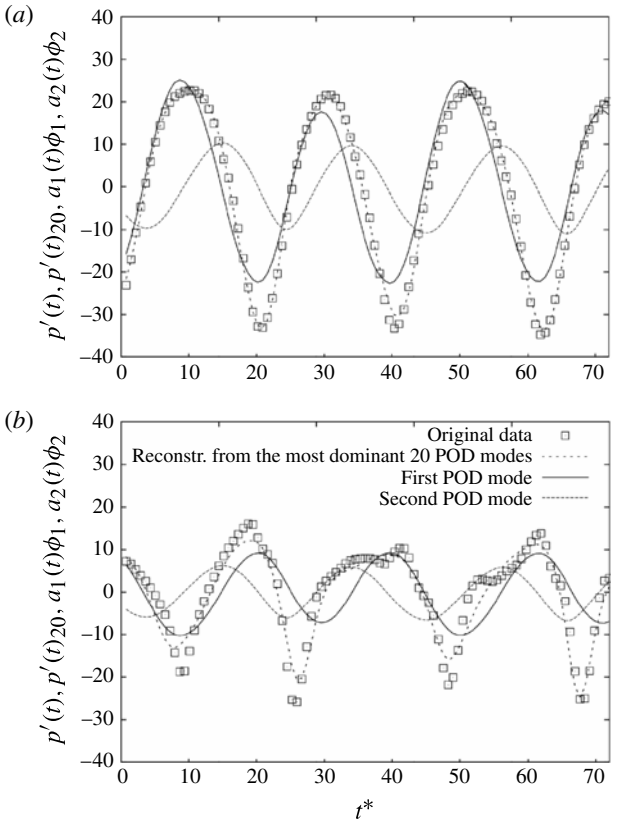

FIGURE 19. Pressure fluctuation, reconstructed pressure fluctuation from the dominant 20 POD modes, and the first and second POD modes at (*a*) $(r, z) = (d_0/2, 0.964L_{im})$ and (*b*) $(r, z) = (d_0/2, 1.238L_{im})$.

accurately at both positions, and therefore these decompositions and reconstructions are conducted correctly. At $(r, z) = (d_0/2, 0.964L_{im})$, the first POD mode is much more dominant than the second POD mode, and the original pressure fluctuation

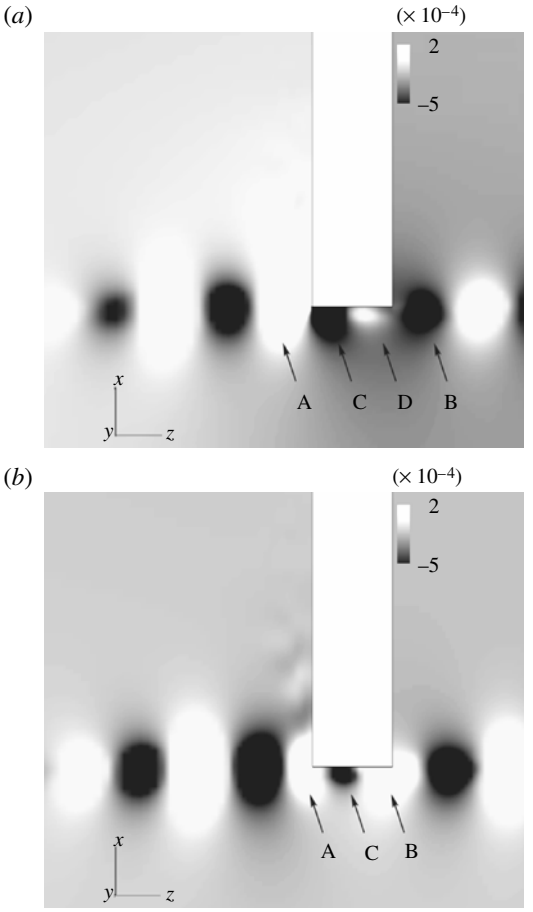

FIGURE 20. The first and second empirical eigenfunctions: (*a*) first mode, (*b*) second mode.

is represented mainly by the first POD mode. At $(r, z) = (d_0/2, 1.238L_{im})$, the first and second POD modes have almost equivalent magnitudes and the difference is the phase between them. Although the positions of the negative peaks of the original data lie between those of the negative peaks of the first and second POD modes, the positive peaks are mainly represented by the first POD mode. Therefore, the first POD mode, which has the most dominant fractional energy, mainly reproduces the pressure fluctuation both upstream and downstream of the end plate hole.

Figure 20 shows the distributions of the first and second eigenfunctions. In the first eigenfunction, there are a high pressure region 'A' on the upstream side of the hole and a low pressure region 'B' on the downstream side of the hole. There is another low pressure region 'C' on the interior side of the upstream edge, and another high pressure region 'D' is formed between low pressure region 'C' and region 'B' on the downstream side of the hole. Therefore, the first eigenfunction is anti-symmetric regarding the pressure distribution between the upstream and downstream sides of the hole. When the dominance of the first POD mode is taken into consideration, this distribution is consistent with the pressure distribution upstream and downstream of the hole observed in § 4.2. In the second eigenfunction, there is a high pressure

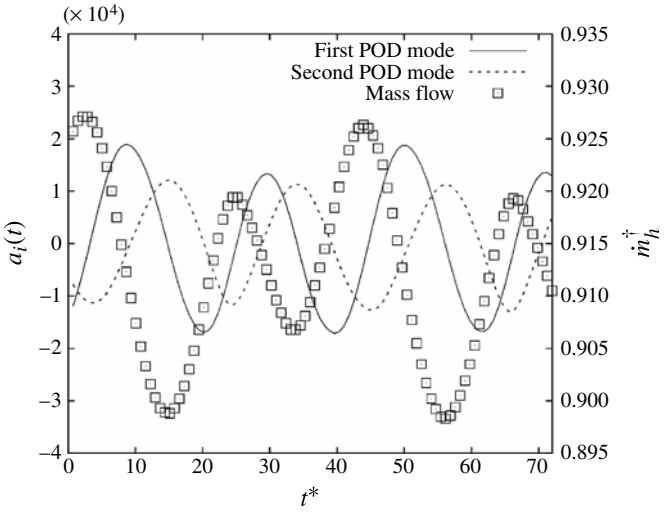

FIGURE 21. Comparison of the time histories of the first and second POD modes' coefficients with that of the mass flow through the end plate hole.

region 'A' on the upstream side of the hole and another high pressure region 'B' on the downstream side of the hole. Between these two high pressure regions, a low pressure region 'C' is formed. Therefore, the second eigenfunction is symmetric regarding the pressure distribution between the upstream and downstream sides of the hole. When the second eigenfunction is compared with the first eigenfunction, the distribution of the second eigenfunction can be viewed as the resulting distribution of the first eigenfunction after a certain time period, i.e. a certain phase shift. In fact, the high pressure region 'A' diminishes from figure 20(*a*) to figure 20(*b*), and high pressure region 'B' in figure 20(*b*) is closer to the hole exit than region 'D' in figure 20(*a*).

Figure 21 shows the comparison of the time histories of the coefficients of the first and second POD modes with those of the mass flow through the end plate hole $\dot{m}_h^\dagger$. When the mass flow is a local minimum the coefficient of the second POD mode becomes a positive peak, and therefore they correlate well. When the coefficient of the second POD mode becomes a peak, that of the first POD mode becomes almost zero. Thus, the mass flow variation is mainly represented by the second POD mode.

Summarizing the above discussion of the first and second POD modes, the pressure fluctuation and the mass flows are respectively expressed by the first and second POD modes, which are mutually orthogonal and have a phase difference of $\pi/2$ similar to the relationship between the sine and cosine functions.

6. An axisymmetric throttling mechanism linking mass flow rates, vortex impingement and global pressure propagation

In §§ 4 and 5 the variation of velocity and pressure fields associated with vortex impingement, i.e. the local phenomena occurring close to the hole edge, pressure wave propagation and the variation of mass flow through the hole were investigated independently. Here, a linkage between these components is investigated, which we name 'the throttling mechanism' in analogy to a mechanical valve that regulates mass

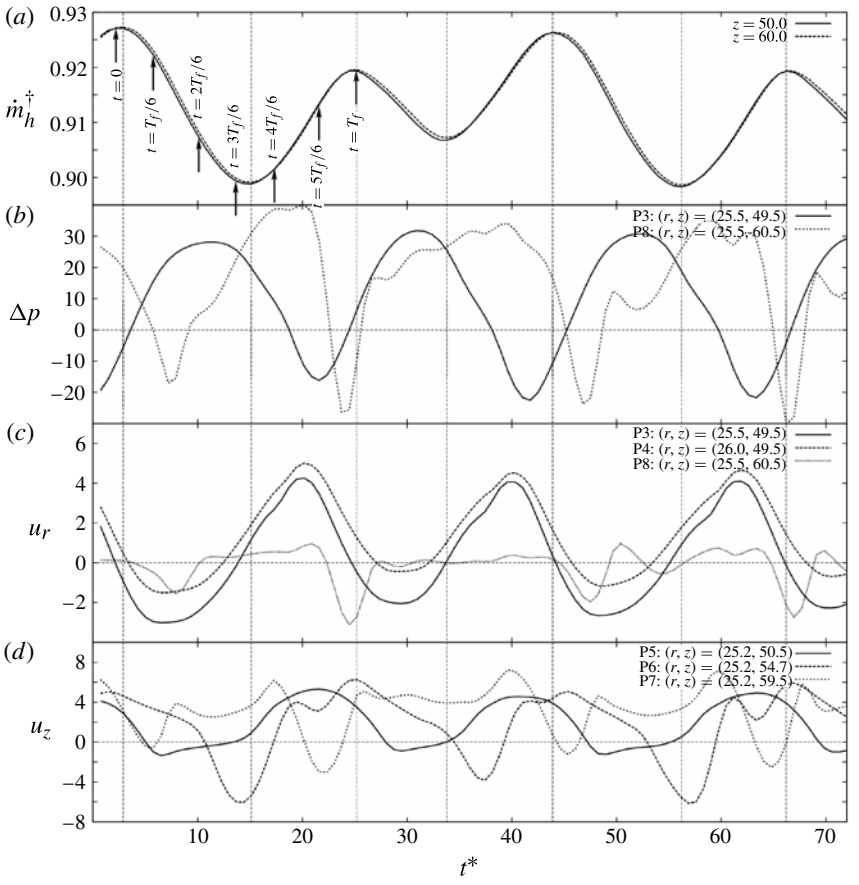

FIGURE 22. Comparisons of (*a*) the time histories of mass flow rates through the end plate hole, (*b*) pressure fluctuation Δp Pa at the inlet and exit of the hole, (*c*) radial velocities u_r m s^{-1} at the inlet and exit of the hole, and (*d*) the streamwise velocities u_z m s^{-1} at the inlet, the centre and the exit of the hole.

flows with its resulting pressure wave propagation. Figure 22 shows comparisons of the time histories of mass flow rates through the end plate hole $\dot{m}_h^\dagger$, pressure fluctuation Δp at the inlet and exit of the hole, radial velocities u_r at the inlet and exit of the hole, and streamwise velocities u_z at the inlet, the centre and the exit of the hole. In the figure, the timings of $t = nT_f/6$ ($n = 0, 1, \ldots, 6$) used in figures 10–12 are also shown. For our convenience, points P3 = (25.5, 49.5), P4 = (26.0, 49.5), P5 = (25.2, 50.5), P6 = (25.2, 54.7), P7 = (25.2, 59.5), P8 = (25.5, 60.5) are defined at $\theta = 0$. Here, $(\cdot, \cdot)$ is the coordinate (r mm, z mm). Figure 23 shows a schematic of the throttling mechanism. Computed pressure contours are partly used in the figure. In the figure, 'H' is a high Δp region and 'L' is a low Δp region.

At $t = 0$, the mass flow rate through the hole $\dot{m}_h^\dagger$ becomes maximal, as shown in figure 22(*a*). From figure 12(*a*) and Δp at P3 in figure 22(*b*), a low pressure region will enter the hole near the hole edge. At this time, u_r at P3 is almost zero, i.e. in parallel to the centreline. Fluid entrainment is facilitated by the small vortex a_2 observed in figure 12(*a*) mentioned previously in § 4.1. At P3 and P4, u_r is on the shift from a positive to negative velocity. As shown in figure 12(*f*), a low pressure region,

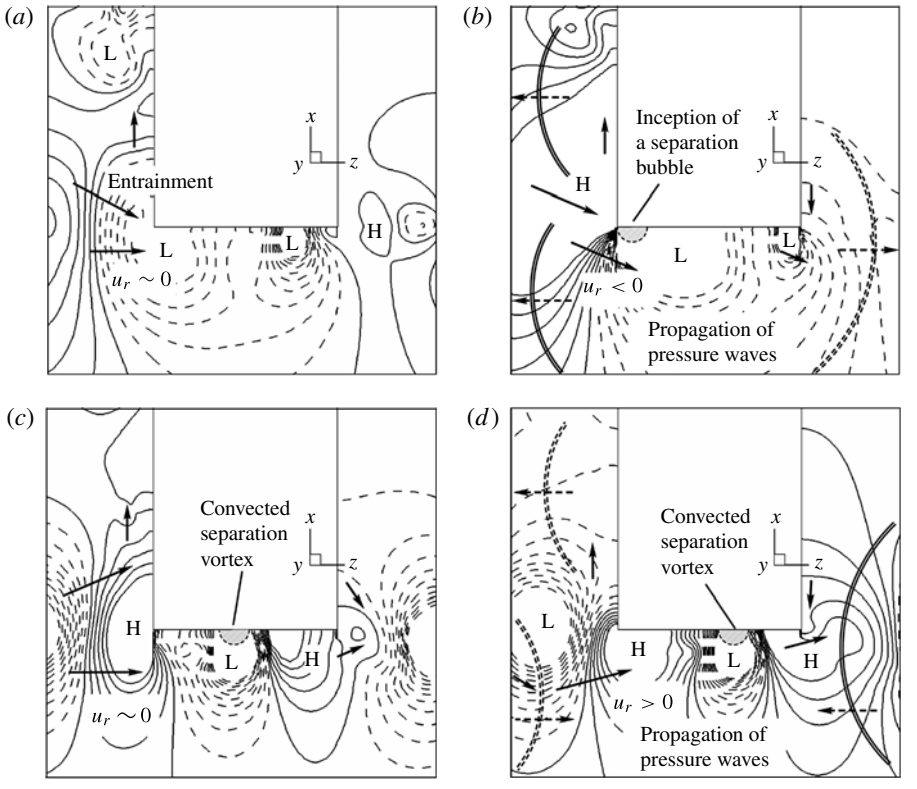

FIGURE 23. An axisymmetric throttling mechanism linking mass flow rates, vortex impingement and global pressure propagation at the end plate hole. H, high Δp; L, low Δp; u_r, the radial velocity; solid lines, positive Δp; dashed lines, negative Δp; double solid lines, compression wave; double dashed lines, expansion wave. (*a*) Maximal $\dot{m}_h$ ($t \sim 0$), (*b*) decreasing $\dot{m}_h$ ($t \sim 0$ to $T_f/6$), (*c*) minimal $\dot{m}_h$ ($t \sim 3T_f/6$), (*d*) increasing $\dot{m}_h$ ($t \sim 3T_f/6$ to $4T_f/6$).

i.e. a vortex with anticlockwise rotation, impinges on the upstream surface of the hole edge just before $\dot{m}_h^\dagger$ becomes maximal, therefore creating the shift from positive to negative velocity mentioned above. At P5, P6 and P7, $u_z > 0$, and therefore no large separation is taking place inside the hole. As mentioned in § 4.1, the separation region k_2 in figure 12(*f*) that was originally formed around $t \sim 2T_f/6$ is now almost as far out of the hole as b_2, although there is no strict repeatability in the positions of b_2 over the successive periods T_f. In § 5, it is shown that the second POD mode correlates well with $\dot{m}_h^\dagger$, and the mode has the symmetric pressure distribution around the hole, as shown in figure 20(*b*). This distribution is consistent with the vortex locations mentioned above, and is the condition for achieving maximal $\dot{m}_h^\dagger$. In figure 16, $t = 0$, i.e. $t^* = 2.16$ corresponds to an intermediate time between a local maximum and minimum pressure, which is also confirmed by Δp at P3 in figure 22(*b*). A schematic of the flow field at $t \sim 0$ is shown in figure 23(*a*).

From $t = 0$ to $\sim T_f/6$, $\dot{m}_h^\dagger$ begins to decrease. As mentioned in § 4.1, a high pressure region starts to impinge on the upstream surface of the hole edge, which is also found in figures 11(*b*), 12(*b*) and 13(*b*,*c*). Associated with the impingement, the ambient Δp increases, by the pressure wave propagation shown in figure 14, in the space between

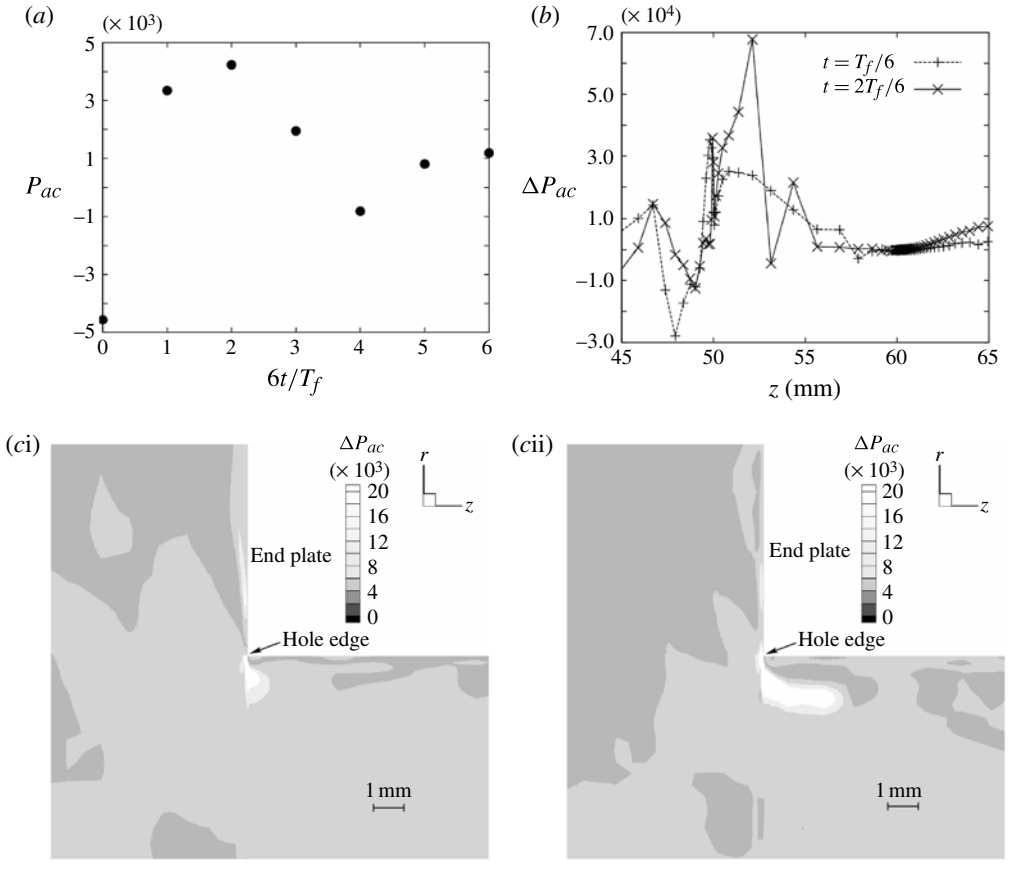

FIGURE 24. Computational results of the instantaneous acoustic power evaluation. (*a*) Instantaneous acoustic power near the hole, P_{ac} W. (*b*) Positional contribution ΔP_{ac} to P_{ac} along the z coordinate at $t = T_f/6$ and $t = 2T_f/6$. (*c*) Spatial contribution $\overline{p_{ac}}$ to P_{ac} around the upstream edge of the hole: (*c*i) $t = T_f/6$, (*c*ii) $t = 2T_f/6$.

the nozzle exit and the end plate, as confirmed in figure 13(*b*,*c*). Because the surface meets the downstream portion of the high pressure region at this time, $u_r < 0$ at P3 and P4, as explained in appendix A. The change of u_r, i.e. the local angle of attack, due to the impingement of the high pressure region is the reason for the decrease of $\dot{m}_h^\dagger$. Because of the negative u_r, the separation bubble d_2 in figure 12(*b*) is formed as mentioned in § 4.1, which is also confirmed by $u_z < 0$ at P5 and $u_z > 0$ at both P6 and P7 in figure 22(*d*). The negative u_r also leads to the negative Δp near the interior surfaces of the hole in figure 13(*b*,*c*), and to the appearance of the region 'A' in figure 16(*a*) associated with the downstream propagation of expansion waves due to the decrease of $\dot{m}_h^\dagger$. The direction of the wave propagation is confirmed by the inclination of contours toward the upper right below region 'A' in figure 16(*a*). It appears that the decrease of $\dot{m}_h^\dagger$ at the hole exit is complemented by the fluid entrainment of vorticity with a separation bubble formed near the upstream edge of the hole. This formation of the separation bubble triggers the decrease of $\dot{m}^\dagger$, i.e. to close the hole in analogy to a mechanical valve. The flow field of $t \sim 0$ to $T_f/6$ is sketched in figure 23(*b*).

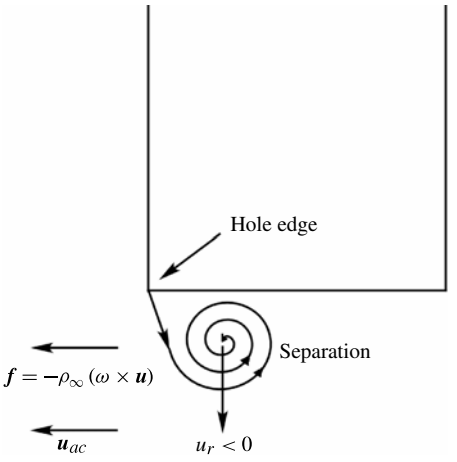

FIGURE 25. Explanation for the strong acoustic power generation.

To identify flow regions responsible for strong sound production, the vortex sound theory developed by Howe (1975, 1980) is used. The procedures to evaluate instantaneous acoustic power are described in appendix B. The results of the evaluation are summarized in figure 24. Figure 24(*a*) shows the instantaneous acoustic power P_{ac} generated in a volume V at $t = nT_f/6$ $(n = 0, 1, \ldots, 6)$. Here,

$$V \equiv \{(r, \theta, z);\ (r, \theta, z) \in V_1 \cup V_2 \cup V_3\}, \tag{6.1}$$

where

$$V_1 \equiv [d_0/51, 4.93d_0] \times [0, 2\pi) \times [45\ \text{mm}, 50\ \text{mm}], \tag{6.2}$$

$$V_2 \equiv [d_0/51, d_0/2] \times [0, 2\pi) \times [50\ \text{mm}, 60\ \text{mm}], \tag{6.3}$$

$$V_3 \equiv [d_0/51, 4.93d_0] \times [0, 2\pi) \times [60\ \text{mm}, 65\ \text{mm}]. \tag{6.4}$$

P_{ac} becomes high around $t = T_f/6$ to $2T_f/6$. Figure 24(*b*) shows positional contribution ΔP_{ac} to P_{ac} along the z coordinate at $t = T_f/6$ and $t = 2T_f/6$. ΔP_{ac} is defined by integrating the power per unit volume p_{ac} in the r, θ directions, i.e.

$$\Delta P_{ac} \equiv \iint \frac{p_{ac}}{J}\, \mathrm{d}\xi\, \mathrm{d}\eta, \quad p_{ac} \equiv -\rho_\infty(\omega \times \boldsymbol{u}) \cdot \boldsymbol{u}_{ac}. \tag{6.5}$$

Here, ξ and η are the general coordinates in the θ and r directions, respectively. High values of ΔP_{ac} are observed around $z = 50$–53 mm. Figure 24(*c*) shows spatial contribution $\overline{p_{ac}}$ to P_{ac} around the upstream edge of the hole at $t = T_f/6$ and $t = 2T_f/6$. $\overline{p_{ac}}$ is defined as the average of p_{ac} in the θ direction. Two high $\overline{p_{ac}}$ regions are observed. The highest $\overline{p_{ac}}$ region coincides with the outer edge of the separation region, and the second highest $\overline{p_{ac}}$ region is on the just upstream side of the end plate near the hole edge. In the former region, considering the vorticity of the region and $u_r < 0$, an external force $\boldsymbol{f} = -\rho_\infty(\omega \times \boldsymbol{u})$ acting on acoustic potential flows is in the $-z$ direction, which coincides with the direction of the pressure wave propagation as in figure 25. Therefore, when § 4.2 is taken into consideration, the outer edge of the separation region near the upstream edge of the hole is considered to be the major sound source of the pressure waves propagating inside the jet. Meanwhile, the upstream side of

the end plate near the hole edge is considered to be the major sound source of the pressure waves propagating outside the jet.

At $t = 2T_f/6$, $\dot{m}_h^\dagger$ is still decreasing. From figure 11(c), the high pressure region near the upstream surface of the hole edge is compressed further than at $t = T_f/6$ by the impingement. In figure 22(b), the pressure at P3 reaches a local maximum. Near the maximal pressure, $|u_r|$ at both P3 and P4 becomes smaller than $|u_r|$ at $t = T_f/6$ because flows from successive low pressure vortices meet at regions where pressure becomes maximal, as explained in appendix A. However, because u_r is still negative, a separation bubble near the hole edge continues to expand, as found from $u_z < 0$ at P5, $u_z \sim 0$ at P6 and $u_z > 0$ at P7 in figure 22(d). By the propagation of compression and expansion waves, region 'A' of $\Delta p < 0$ and region 'B' of $\Delta p > 0$ in figure 16 are clearly formed at this time, which is also confirmed by figure 13(c,d). The pressure distribution at this time is dominantly represented by the eigenfunction of the first POD mode based on the discussion in § 5. Region 'A' in figure 16(a) corresponds to the formation of the low pressure regions 'B' and 'C' in figure 20(a), which is also confirmed by figure 13(c,d), and region 'B' in figure 16(a) corresponds to the formation of the high pressure region 'A' in figure 20(a) by the impingement. Region 'B' in the eigenfunction corresponds to the vortices observed in figure 12(b,c).

At $t = 3T_f/6$, $\dot{m}_h^\dagger$ becomes a local minimum. From figures 11(d) and 12(d), the high pressure regions near the upstream surface of the hole edge are diminished compared to $t = 2T_f/6$, and the pressure at P3 starts to decrease from the maximal pressure at $t = 2T_f/6$ in figure 22(b). Because $u_r \sim 0$ at P3, as shown in figure 22(c), the centre of the high pressure region is almost at the edge based on the discussion in appendix A. However, because the surrounding flows have outward components due to the existence of a low pressure region upstream of the high pressure region as also mentioned in § 4.1, the fluid entrainment observed in figures 11(a) and 12(a) does not occur, and therefore $\dot{m}_h^\dagger$ becomes minimal. Because $u_r \sim 0$, the separation bubble at the upstream side of the hole disappears, as found in $u_z \sim 0$ at P5. Compared with $t = 2T_f/6$, the separation bubble is convected downstream to the middle of the hole, as found both from figure 12(d) and from $u_z < 0$ at P6 and $u_z > 0$ at P7 in figure 22(d). Because the variation of $\dot{m}_h^\dagger$ correlates well with the second POD mode as discussed in § 5, the pressure distribution around the hole in figure 13(e) is very similar to that in figure 20(b). The low pressure region 'C' in figure 20(b) corresponds to the convected separation bubble mention above. Between the low pressure region at the middle of the hole, and a vortex downstream of the edge, a high pressure region is formed at the exit of the edge, which is shown as 'B' in figure 20(b). It corresponds to the appearance of high pressure region 'C' in figure 16(a). The increase of pressure at the downstream edge of the hole, which is also confirmed by Δp at P8, correlates well with the increase of u_r at the same point. The flow field at the time is sketched in figure 23(c).

From $t = 3T_f/6$ to $\sim 4T_f/6$, $\dot{m}_h^\dagger$ starts to increase, which corresponds to the start of opening the hole in analogy to a mechanical valve. The high pressure region will enter the hole in figure 12(e), and a low pressure region with anticlockwise rotation is approaching from upstream to the edge in figure 11(e). As a result, the pressure at P3 decreases, and u_r also increases continuously with the entrainment of the surrounding fluids to the hole, which is the reason for the increase in $\dot{m}_h^\dagger$. Accompanying the pressure decrease near the hole, the ambient pressure upstream of the end plate decreases almost simultaneously, which is confirmed by figure 13(e,f), figures 15 and 16(a). The separation region inside the hole is convected further downstream than $t = 3T_f/6$, and the upstream end of the region is around $z \sim 54.7$ mm, as found

from $u_z \sim 0$ in figure 22(*d*). Increasing $\dot{m}_h^\dagger$ makes the u_r of outflows positive, which results in the high pressure region downstream of the edge, and is consistent with the distribution of the first POD mode's eigenfunction. With the growth of the high pressure region near the downstream surface of the edge, which is also found by the increase of Δp at P8, the ambient pressure downstream of the end plate becomes high, which is confirmed by region 'C' in figure 16(*a*). Compression waves propagate upstream, as found by the inclination of contours toward upper left below region 'C' in figure 16(*a*). The flow fields for $t = 3T_f/6$ to $4T_f/6$ are sketched in figure 23(*d*).

At $t = 5T_f/6$, $\dot{m}_h^\dagger$ is still increasing. A low pressure region impinges on the hole edge, as found from figure 12(*f*), figure 13(*g*,*h*), and the minimal value of Δp at P3. Because of the vorticity of the low pressure region, u_r at P3 and P4 becomes a local maximum. Consistent with the dominance of the first POD mode and its eigenfunction in figure 20(*a*), the pressure at the exit of the hole becomes a local maximum as opposed to the minimal pressure at the upstream edge, which is confirmed by Δp at P8 in figure 20(*b*). The separation region inside the hole is convected near the exit, as found from $u_z < 0$ at P7. Due to the large u_r near the upstream side of the hole edge, a portion of a vortex in the jet shear layer does not enter the hole and is ejected in the radial direction near the upstream surface of the end plate, which was mentioned previously as b_1 in figure 11(*a*). At $t = 6T_f/6$ the flow states come back to similar states as at $t = 0$.

7. Conclusions

Direct computations of a hole tone feedback system were conducted. The mean velocity of an air jet was 10 m s^{-1}. The diameters of the nozzle and the end plate hole used were both 51 mm, and the impingement length between the nozzle and the end plate was 50 mm. This numerical method was validated against past experimental data in terms of the qualitative vortical structures, the relationship between the most dominant hole tone peak frequency and the jet speed, and the downstream growth of the mean jet profiles. Based on the computational results, the shear-layer impingement on the hole edge, the resulting propagation of the pressure waves and the associated vortical structures were discussed. In the jet shear layers, successive high and low pressure regions were formed. A simple explanation for the generation of the high pressure region and the directions of velocity vectors between two low pressure regions with backflows were given based on potential flow theory. The periodic pressure fluctuation as a result of shear-layer instability around the jet is associated with the variation of velocity vectors. Therefore, the shear-layer impingement on the hole edge is associated with the periodic flow separation and reattachment near the edge due to the variation of incidence angles to the edge. Accompanying the events, high and low pressure regions appeared alternately over a wide area upstream and downstream of the end plate hole. Dominant pressure fluctuations propagated both inside and outside the jet, and the frequencies of the pressure fluctuations coincided with those of successive vortices in the jet shear layer. Inside the jet, the directions of the pressure wave propagation differed between the compression and expansion processes.

To extract the dominant unsteady behaviours of the hole tone phenomenon, a snapshot POD analysis of the pressure fluctuation fields was conducted. The first and second eigenfunctions were respectively anti-symmetric and symmetric with regard to the pressure distribution around the hole. The pressure fluctuations and the mass flows were dominantly expressed by the first and second POD modes, respectively, which

had a phase difference of $\pi/2$ similar to the relationship between the sine and cosine functions.

Integrating the computational results, an axisymmetric throttling mechanism linking the mass flow rates through the hole, the vortex impingement and the global pressure propagation is proposed. When a low pressure region entered the hole at $t = 0$, flows entered the hole almost in parallel to the centreline. In addition, the low pressure region had vorticity, which augments the surrounding fluid entrainment. Consequently, the mass flow rates through the hole, i.e. $\dot{m}_h$, became maximal at this stage. Around $t = T_f/6$ to $2T_f/6$, the downstream half portion of a high pressure region impinged on the upstream surface of the hole edge. Because the velocity vectors of the region had inward components, i.e. $u_r < 0$, meaning the formation of the separation bubble at the hole edge, $\dot{m}_h$ started to decrease compared with that at $t = 0$. Because the flows were blocked by the surface of the edge, a high pressure region grew on the surface. As a result, especially around $t \sim T_f/6$, compression waves propagated upstream both inside and outside the jet between the nozzle exit and the end plate. Meanwhile, expansion waves propagated downstream of the end plate because $\dot{m}_h$ decreased. Near the downstream edge of the hole, low pressure vortical flows with $u_r < 0$, which were similar to the distribution of the eigenfunction of the first POD mode, were realized. The outer edge of the separation region and the upstream side of the hole edge produce strong sound. Around $t = 3T_f/6$, the centre of the high pressure region, which has $u_r \sim 0$ was almost at the edge. However, because the surrounding flows had outward components due to the existence of a low pressure region upstream of the high pressure region, $\dot{m}_h$ became minimal. Around $t = 4T_f/6$ to $5T_f/6$, a low pressure region impinged on the upstream surface of the hole edge. Because the velocity vectors had outward components, i.e. $u_r > 0$ due to the vorticity of the low pressure region, $\dot{m}_h$ also started to increase with entrainments of the surrounding flows compared with that at $t = 3T_f/6$. Especially around $t \sim 4T_f/6$, expansion waves propagated upstream outside the jet and downstream inside the jet by the impingement. Near the downstream edge of the hole, increasing $\dot{m}$ made the u_r of outflows positive, which resulted in a high pressure region downstream of the edge. As a result, compression waves propagated upstream towards the end plate hole. It was consistent with the distribution of the eigenfunction of the first POD mode.

Acknowledgements

This research was supported by the Global COE Program 'World Center for Education and Research for Trans-disciplinary Flow Dynamics', of Tohoku University. Computational resources were provided by the Advanced Fluid Information Research Center of the Institute of Fluid Science, and also by the Cyberscience Center, Tohoku University. The experiment was conducted with the cooperation of Mr A. Totsuka, a technician at the Institute of Fluid Science, Tohoku University.

Appendix A. A simple explanation for the generation of a high pressure region, and the direction of velocity vectors between vortices

As mentioned in § 4.1, successive high and low pressure regions are formed in the jet shear layers. The low pressure regions correspond to vortices with backflows. Here, we explain, by a simple model based on potential flow theory, the generation of such high pressure regions between successive vortices. In addition, the direction of velocity vectors between the vortices is also discussed. Assuming two free vortices with constant circulation Γ which are at a distance of λ from each other, the complex

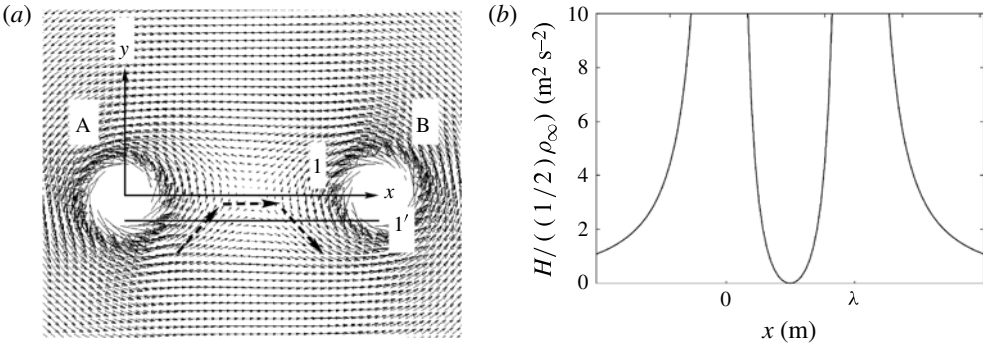

FIGURE 26. A vector field and dynamic pressure distribution formed by two free vortices: (*a*) vector field; (*b*) distribution of dynamic pressure divided by $(1/2)\rho_\infty$.

potential $W(z)$ becomes (Imai 1973)

$$W(z) = \frac{\Gamma}{2\pi \mathrm{i}}(\ln(z) + \ln(z-\lambda)). \tag{A 1}$$

Inserting $z = r\mathrm{e}^{\mathrm{i}\theta}$, the complex velocity reads

$$\frac{\mathrm{d}W(z)}{\mathrm{d}z} = u - \mathrm{i}v = \frac{\Gamma}{2\pi \mathrm{i}}\left(\frac{1}{z} + \frac{1}{z-\lambda}\right) \tag{A 2}$$

$$= -\frac{\Gamma \sin\theta}{2\pi}\left\{\frac{1}{r} + \frac{r}{(r\cos\theta-\lambda)^2 + (r\sin\theta)^2}\right\} - \mathrm{i}\frac{\Gamma}{2\pi}\left\{\frac{\cos\theta}{r} + \frac{r\cos\theta-\lambda}{(r\cos\theta-\lambda)^2 + (r\sin\theta)^2}\right\}. \tag{A 3}$$

The resulting dynamic pressure $\mathscr{H}$ becomes

$$\mathscr{H} = \frac{1}{2}\rho_\infty(u^2+v^2) \tag{A 4}$$

$$= \frac{1}{2}\rho_\infty\left(\frac{\Gamma}{2\pi}\right)^2\left\{\frac{1}{r^2} + \frac{1}{(r\cos\theta-a)^2 + (r\sin\theta)^2} + \left(\frac{2}{r}\right)\frac{r-a\cos\theta}{(r\cos\theta-a)^2 + (r\sin\theta)^2}\right\}. \tag{A 5}$$

Figure 26 shows a vector field and dynamic pressure distribution formed by the two free vortices. To plot the figure, $\lambda = 14.4 \times 10^{-3}$ m, and $\Gamma = 2\pi R v_\theta$ with $R = 2 \times 10^{-3}$ m and $v_\theta = 5$ m s^{-1} are substituted based on the computed flow results. In figure 26(*a*), because vector fields become singular around the vortex cores $x = 0, \lambda$, the vectors near the cores are removed from the figure. In figure 26(*b*), the dynamic pressure becomes low between the vortices, and therefore the static pressure becomes high according to Bernoulli's principle.

Another important property of the vortex system is that, on the line l' which is below the line l, $u_x > 0$ and $u_y > 0$ near A, $u_y \sim 0$ near the centre between A and B where the pressure becomes high, and $u_x > 0$ and $u_y < 0$ near B.

Appendix B. Evaluation of instantaneous acoustic power

In order to identify flow regions responsible for strong sound production, the vortex sound theory developed by Howe (1975, 1980) is used. The theory shows that when an acoustic oscillation occurs in an inviscid, isentropic but rotational flow, then instantaneous acoustic power P_{ac} is generated in a volume V, which is given by

$$P_{ac} = -\rho_\infty \int_V (\omega \times \boldsymbol{u}) \cdot \boldsymbol{u}_{ac} \, \mathrm{d}V, \tag{B 1}$$

where $\boldsymbol{u}$ is the instantaneous fluid velocity, $\omega = \nabla \times \boldsymbol{u}$ is the vorticity, $\boldsymbol{u}_{ac}$ is the acoustic particle velocity, and ρ_∞ is the mean density of the fluid. The acoustic particle velocity is defined as the fluctuating irrotational part of the flow field (Howe 1997*a*), and is obtained by the following procedure. By the Helmholtz–Hodge decomposition (Chorin & Marsden 1992), the fluid velocity $\boldsymbol{u}$ is uniquely decomposed into the irrotational and the solenoidal parts as

$$\boldsymbol{u} = \nabla\phi + \nabla \times \boldsymbol{A}, \quad \nabla \cdot \boldsymbol{A} = 0. \tag{B 2}$$

Here, ϕ and $\boldsymbol{A}$ are a scalar potential and a vector potential, respectively. ϕ is obtained by solving the following Poisson equation in a domain Ω with corresponding boundary conditions:

$$\nabla^2\phi = \nabla \cdot \boldsymbol{u} \quad \text{in } \Omega, \quad \boldsymbol{n} \cdot \nabla\phi = \boldsymbol{n} \cdot \boldsymbol{u} \quad \text{on } \partial\Omega. \tag{B 3}$$

Here, $\boldsymbol{n}$ is the unit normal vector directed outward from $\partial\Omega$. While the domain Ω where the Poisson equation is solved has the same multidomain configuration as figure 2, the far boundaries in the r and z directions are trimmed to $r = 4.93d_0$ and $z = 4.03d_0$ to reduce computational cost. In addition, grid A mentioned in § 2.2 is used. The velocity fields are interpolated from grid B. Because ϕ has an arbitrariness of a constant, the value of ϕ at a reference point is fixed. The above decomposition is conducted also for the time-averaged velocity field $\boldsymbol{u}_0$, and its scalar potential ϕ_0 is obtained. Finally, $\boldsymbol{u}_{ac}$ is defined by

$$\boldsymbol{u}_{ac} = \nabla(\phi - \phi_0). \tag{B 4}$$

REFERENCES

BLAKE, W. K. 1986 *Mechanics of Flow-Induced Sound and Vibration,* vol. 1. Academic.

CHANAUD, R. C. & POWELL, A. 1965 Some experiments concerning the hole and ring tone. *J. Acoust. Soc. Am.* **37** (5), 902–911.

CHORIN, A. & MARSDEN, J. 1992 *A Mathematical Introduction to Fluid Mechanics*. Springer.

CRIGHTON, D. G. 1992 The jet edge-tone feedback cycle: linear theory for the operating stages. *J. Fluid Mech.* **234**, 361–391.

FREUND, J. B. 1997 Proposed inflow/outflow boundary condition for direct computation of aerodynamic sound. *AIAA J.* **35** (4), 740–742.

GAITONDE, D. V. & VISBAL, M. R. 2000 Padé-type higher-order boundary filters for the Navier–Stokes equations. *AIAA J.* **38** (11), 2103–2112.

GINEVSKY, A. S., VLASOV, Y. V. & KARAVOSOV, R. K. 2010 *Acoustic Control of Turbulent Jets*. Springer.

HOLGER, D. K. 1977 Fluid mechanics of the edgetone. *J. Acoust. Soc. Am.* **62** (5), 1116–1128.

HOWE, M. S. 1975 Contributions to the theory of aerodynamic sound, with application to excess jet noise and the theory of the flute. *J. Fluid Mech.* **71**, 625–673.

HOWE, M. S. 1980 The dissipation of sound at an edge. *J. Sound Vib.* **70** (3), 407–411.

HOWE, M. S. 1997*a* *Acoustics of Fluid–Structure Interactions*. Cambridge University Press.

HOWE, M. S. 1997*b* Edge, cavity and aperture tones at very low Mach numbers. *J. Fluid Mech.* **330**, 61–84.

IMAI, I. 1973 *Fluid Dynamics,* vol. 1. Syokabo.

LANGTHJEM, M. A. & NAKANO, M. 2005 A numerical simulation of the hole-tone feedback cycle based on an axisymmetric discrete vortex method and Curle's equation. *J. Sound Vib.* **288** (1–2), 133–176.

LELE, S. K. 1992 Compact finite difference schemes with spectral-like resolution. *J. Comput. Phys.* **103** (1), 16–42.

MATSUURA, K. & KATO, C. 2007 Large-eddy simulation of compressible transitional flows in a low-pressure turbine cascade. *AIAA J.* **45** (2), 442–457.

MATSUURA, K. & NAKANO, M. 2011 Direct computation of a hole-tone feedback system at very low Mach numbers. *J. Fluid Sci. Technol.* **6** (4), 548–561.

MICHALKE, A. 1984 Survey on jet instability theory. *Prog. Aerosp.* **21**, 159–199.

PRESS, W. H., TEUKOLSKY, S. A., VETTERLING, W. T. & FLANNERY, B. P. 1992 *Numerical Recipes in Fortran 77*, second edition. Cambridge University Press.

RAI, M. M. & MOIN, P. 1993 Direct numerical simulation of transition and turbulence in a spatially evolving boundary layer. *J. Comput. Phys.* **109** (2), 169–192.

RAYLEIGH, LORD. 1945 *Theory of Sound,* vol. 2. Dover.

ROCKWELL, D. & NAUDASCHER, E. 1979 Self-sustained oscillations of impinging free shear layers. *Annu. Rev. Fluid Mech.* **11**, 67–94.

ROSSITER, J. E. 1962 The effect of cavities on the buffeting of aircraft. Royal Aircraft Establishment Technical Memorandum 754.

SIROVICH, L. & RODRIGUEZ, J. D. 1987 Coherent structures and chaos: a model problem. *Phys. Lett.* A **120** (5), 211–214.

SONDHAUSS, C. 1854 Ueber die beim Ausströmen der Luft enstehenden Töne. *Ann. Phys.* **167** (1), 126–147.

STUDENT 1908 The probable error of a mean. *Biometrika* **6** (1), 1–25.

UMEDA, Y. & ISHII, R. 1986 Frequency characteristics of discrete tones generated in a high subsonic jet. *AIAA J.* 693–695.